Laboratory VIS–NIR reflectance measurements of heated Vesta regolith analogs: Unraveling the spectral properties of the pitted impact deposits on Vesta

T. MICHALIK [1,2]*, A. MATURILLI[1], E. A. CLOUTIS[3], K. STEPHAN [1], R. MILKE[4],
K.-D. MATZ[1], R. JAUMANN[4], L. HECHT[2], H. HIESINGER[5], and K. A. OTTO[1]

[1]Institut für Planetenforschung, Deutsches Zentrum für Luft- und Raumfahrt e.V., Berlin, Germany
[2]Leibniz-Institut für Evolutions- und Biodiversitätsforschung, Museum für Naturkunde, Berlin, Germany
[3]Department of Geography, University of Winnipeg, Winnipeg, Manitoba, Canada
[4]Institut für Geologische Wissenschaften, Freie Universität Berlin, Berlin, Germany
[5]Institut für Planetologie, Westfälische Wilhelms-Universität, Münster, Germany
*Correspondence
T. Michalik, Leibnitz-Institut für Evolutions- und Biodiversitätsforschung, Invalidenstr. 43, 10115 Berlin, Germany.
Email: tanja.michalik@mfn-berlin.de

Abstract–Pitted impact deposits on Vesta show higher reflectance and pyroxene absorption band strengths compared to their immediate surroundings and other typical Vestan materials. We investigated whether heating to different temperatures for different durations of Vestan regolith analog materials can reproduce these spectral characteristics using mixtures of HEDs, the carbonaceous chondrite Murchison, and terrestrial analogs. We find no consistent spectral trend due merely to temperature increases, but observed that the interiors of many heated samples show both higher reflectance and pyroxene band I strength than their heated surfaces. With electron probe microanalysis, we additionally observe the formation of hematite, which could account for the higher reflectance. The presence of hematite indicates oxidation occurring in the sample interiors. In combination with heat, this might cause the increase of pyroxene band strengths through migration of iron cations. The effect grows larger with increasing temperature and duration, although temperature appears to play the more dominant role. A higher proportion of Murchison or the terrestrial carbonaceous chondrite analog within our mixtures also appears to facilitate the onset of oxidation. Our observations suggest that both the introduction of exogenic material on Vesta as well as the heating from impacts were necessary to enable the process (possibly oxidation) causing the observed spectral changes.

INTRODUCTION

Pitted impact deposits (PIDs) are geomorphologies showing dense clusters of polygonally shaped pits and were linked to the rapid loss of volatiles, probably due to impact heating (Denevi et al., 2012; Tornabene et al., 2012). They have been recognized and analyzed so far on Mars (e.g., Boyce et al., 2012; Tornabene et al., 2012), Vesta (e.g., Denevi et al., 2012; Michalik et al., 2021; Michalik, Stephan, et al., 2022) as well as Ceres (e.g., Sizemore et al., 2017) and occur within and around impact craters. Additionally, the volatiles lost at the PIDs' sites have been attributed to the target material, that is, the ice-rich subsurface of Mars (Tornabene et al., 2012) or the possibly water ice-bearing subsurface of Ceres (Sizemore et al., 2017). In the case of Vesta, the volatiles shaping PIDs are attributed to exogenic carbonaceous chondrite-bearing material (Denevi et al., 2012; Michalik et al., 2021). Vesta is generally thought to be differentiated (e.g., Consolmagno & Drake, 1977; Keil, 2002; Larson & Fink, 1975; McCord et al., 1970; Mittlefehldt, 2015; Ruzicka et al., 1997; and references

therein) as shown by analysis of HED meteorites (howardites, eucrites, diogenites) and ground-based observational data. The Dawn mission revealed that Vesta's surface is contaminated by carbonaceous chondrite material through influx over geological time scales (e.g., De Sanctis, Combe, et al., 2012; Jaumann et al., 2014; McCord et al., 2012; Palomba et al., 2014; Reddy et al., 2012) (possibly among other meteorite types). The volatiles needed to form the PIDs on Vesta therefore likely originated from exogenous impactors carrying hydrated phases (Denevi et al., 2012; Michalik et al., 2021). Comets or endogenic icy sources on the other hand are unlikely sources for the PIDs on Vesta due to their very high impact velocities (Denevi et al., 2012) and the fact that PIDs form as a result of accumulation of ejecta within or at topographic traps like craters and/or scarps/ridges (Michalik et al., 2021).

Based on Dawn Framing Camera (FC) and visible and infrared spectrometer (VIR) data, Michalik et al. (2021) and Michalik, Stephan, et al. (2022) investigated the spectral properties of the PIDs, focusing on those located around the large (~60 km), well-preserved crater Marcia in the equatorial region of Vesta. The PIDs exhibit higher overall reflectance and higher pyroxene band strengths with respect to their immediate impact deposit surrounding (Figure 1c), based on the VNIR reflectance and band strengths of the two spin-allowed pyroxene crystal field absorptions near 0.9 and 1.9 μm. Figure 1 shows examples of the PIDs spectral characteristics focusing on the reflectance in the visible light and the pyroxene band I absorption near 0.9 μm. Furthermore, a local OH depletion at the PIDs' sites, derived from Dawn VIR data (Combe et al., 2015), can be observed (Figure 1, 3rd panel in upper rows; Michalik et al., 2021).

These spectral characteristics are inconsistent with variations in grain size, age, roughness, shock state, or glass content (Michalik et al., 2021). As grain sizes increase, overall reflectance in the visible wavelength region commonly increases as well, while band strengths decrease (e.g., Adams & Filice, 1967; Burbine et al., 2001; Clark, 1999; Cloutis et al., 2013), which contradicts our observations of PIDs. As roughness tends to behave in similar ways (Harloff & Arnold, 2001), this possibility was also excluded. The study about glass content and its effect on spectral characteristics by Tompkins and Pieters (2010) suggests that variations in glass content neither play a role. The results of Cloutis et al. (2013) indicate that variations in shock state, number of opaque phases, and plagioclase content are also unlikely candidates for creating higher reflectances and pyroxene band strengths. Finally, as PIDs occur within a larger, otherwise smooth and darker ejecta deposit, differences in age can likely be excluded. PIDs were probably formed within hours, days, or weeks after deposition of the whole ejecta deposit (Boyce et al., 2012; Michalik et al., 2021; Tornabene et al., 2012), leaving them to experience basically the same amount of space weathering and other forces when considering geological time scales (crater Marcia was formed around 40–390 Ma ago; Williams, Jaumann, et al., 2014).

On the basis of Dawn VIR observations and preliminary work of this study (Michalik, Maturilli, et al., 2022), Michalik, Stephan, et al. (2022) suggested that a form of oxidation occurring within the ejecta is causing this phenomenon. This oxidation could provoke the redistribution of iron cations within the pyroxene crystals and change their spectral properties. The oxidation process is possibly enabled due to impact heat, the presence of hydrated material in the Vestan regolith (providing the necessary volatiles), and the entrapment of material so that volatiles are not immediately lost to space, yet being able to interact with their surrounding material. Based on a calculation presented by Reddy et al. (2012), Michalik et al. (2021) estimated carbonaceous chondrite-type CM2 abundances of about 10–30 vol% in the Marcia ejecta blanket, providing enough volatiles for such processes. Most importantly to note, solid particles were likely released from the interior deposit along with volatiles during the formation of PIDs (Boyce et al., 2012), thus exposing this secondarily altered material at the surface.

In this study, we investigated whether heating of terrestrial and meteoritic analogs of the Vestan regolith could result in such higher reflectance and pyroxene band strength. We heated these analogs to various temperatures and durations. There are no studies estimating the temperatures reached during the Marcia impact or within the ejecta deposits external to the crater. However, Williams, O'Brien, et al. (2014) estimate melt production rates for Marcia and find that impact melt could have been emplaced beyond the crater rim with quantities up to 11 km^3. Thus, initial temperatures of such deposits might have been sufficiently high (≥400°C). Depending on the deposit thickness, cooling might also have been slow enough for alteration processes to occur. Moreover, Boyce et al. (2012) showed that for PIDs associated with Tooting crater (Mars) and an estimated volatile content of 10% by mass of water, the devolatilization process and/or pit formation ceased after ~96 days. For an estimated volatile content of 4%, they state that this value decreases to ~38 days. Another decrease of devolatilization time could occur due to the decrease of median clast size in their calculations, leading to a cessation of steam release after 16 days. As the Vestan regolith holds significantly lower volatile contents, this value might decrease even more. In addition, the lower gravity regime might additionally increase steam
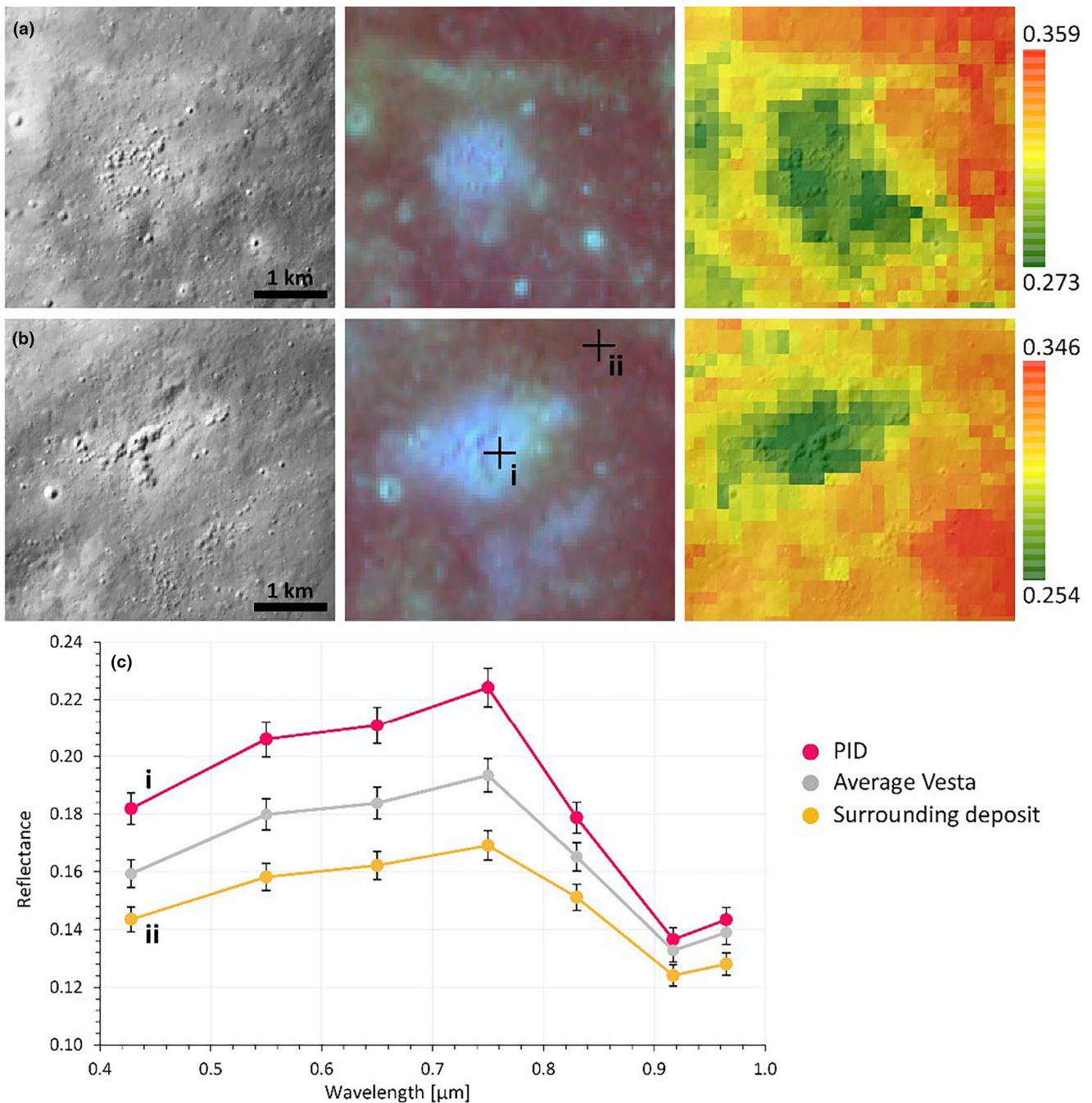
FIGURE 1. Upper two rows (a, b): Two examples of PIDs on Vesta, both appear southwest of Marcia near 1°N and 180°E (Claudia Coordinate System). The first panel in each row shows Dawn FC clear filter data in low-altitude mapping orbit resolution (up to 16 m pixel^{-1}). The second panel shows a RGB composite at high-altitude mapping orbit resolution (up to 60 m pixel^{-1}) with $R = 0.965/0.917$ [μm], $G = 0.750$ μm and $B = 0.750/0.917$ [μm]. Cyan colors indicate higher reflectance and pyroxene band I strengths (located near 0.9 μm). The third panel shows Dawn VIR 2.8 μm band depth data from Combe et al. (2015), with greenish colors indicating less OH. The lower diagram (c) shows an example spectrum of a PID and its surrounding impact deposit from DAWN FC data with i and ii linking the spectra and the location in row (b), second panel. The spectra illustrate the high reflectance and pyroxene band I strength of the PID. The reader is kindly referred to Michalik et al. (2021) and Michalik, Stephan, et al. (2022) for further details. (Color figure can be viewed at wileyonlinelibrary.com)

escape velocities further (Boyce et al., 2012). This results in possibly just hours to days of volatile release at PID sites on Vesta. Therefore, we chose to heat our samples to short (2 h), intermediate (72 h), and long (168 h) heating durations to also evaluate the role of heating duration.

Heating of comet-like and asteroid-like volatile-bearing materials has generally been shown to result in lower reflectance and subdued absorption bands in the visible and near-infrared region (e.g., Alemanno et al., 2020; Galiano et al., 2020; Hiroi & Zolensky, 1999; Poch et al., 2016). These observations make the spectral appearance of the PIDs on Vesta quite unusual and triggered our interest in further investigating this phenomenon. After Michalik et al. (2021) and Michalik, Stephan, et al. (2022), we complement the investigation of the PIDs' distinct spectral characteristics with this laboratory study. As PIDs likely represent windows into the interior of these deposits, we also display reflectance spectra of both surfaces and interiors of the heated samples, possibly analogous to the surface and interiors of ejecta deposits showing PIDs. The heating experiments were conducted in the planetary emissivity laboratory (Helbert & Maturilli, 2008) and the subsequent reflectance measurements were undertaken in the planetary spectroscopy laboratory (Maturilli et al., 2019), both located at the German Aerospace Center (DLR) in Berlin.

DATA AND METHODS

Analog Materials

We generated both terrestrial and meteorite analogs to resemble the Vestan regolith. The Vestan regolith consists of the endogenic eucritic and diogenitic lithologies and likely several exogenic components like, for example, chondritic material. As we observe elevated OH contents in the Marcia area (e.g., Combe et al., 2015; De Sanctis, Combe, et al., 2012), carbonaceous chondrites are likely the most common type on Vesta's surface. Therefore, our analog samples used here comprise an "endogenic," pyroxene-rich portion and an "exogenic," dark, carbonaceous chondrite-like portion. The analogs and their mixture proportions are listed in Table 1. For mixtures of an HED and Murchison, we include the letter "M" after the HED sample name. The exogenic part of the terrestrial analog is an artificially mixed "Phobos Simulant" called UTPS-TB (University of Tokyo Phobos Simulant Tagish Lake-based) which was initially developed as a carbonaceous chondrite (CC) analog for the MMX mission (Martian Moons eXploration) led by JAXA (Japan Aerospace Exploration Agency, Miyamoto et al., 2021). This CC analog was assembled based on Tagish Lake mineralogy, a C2

TABLE 1. Sample materials and their proportions.

Sample name	Endogenic analog	wt %	Exogenic analog	wt %
Hypersthene	Hypersthene	100	–	0
Phobos Simulant	–	0	Phobos Simulant	100
Murchison	–	0	Murchison	100
NWA 3359	NWA 3359	100	–	0
NWA 5748	NWA 5748	100	–	0
NWA 5748M[a]	NWA 5748	80	Murchison	20
NWA 5230M[a]	NWA 5230	85	Murchison	15
JaH 626M[a]	JaH 626	85	Murchison	15
H90P10	Hypersthene	90	Phobos Simulant	10
H80P20	Hypersthene	80	Phobos Simulant	20
H70P30	Hypersthene	70	Phobos Simulant	30

[a]The M denotes that the meteorite is mixed with Murchison.

ungrouped carbonaceous chondrite and contains 60.5 wt % of phyllosilicate, 10.3 wt% of carbonate, 9.2 wt% of sulfide, 7.7 wt% of magnetite, 7.3 wt% of olivine, and roughly 5 wt% of carbon (including polymer organic materials) (Miyamoto et al., 2021). The exogenic meteorite regolith analog that was used is Murchison, a CM2-type carbonaceous chondrite. It consists of roughly 72% matrix and 28% inclusions (Fendrich & Ebel, 2021). The total mineral composition is as follows: cronstedtite/tochilinite (matrix, 58.5%), serpentine (22.8%), olivine (11.6%), pyrrhotite (2.9%), enstatite (2.2%), calcite (1.1%), pentlandite (0.5%), and magnetite (0.4%) (Bland et al., 2004) while chondrules appear to make up at least 12% of Murchison (Fendrich & Ebel, 2021; McSween, 1979). Murchison is very well suited in these experiments as it has been shown that CM2 chondritic clasts are the most common clast types (>80%) in HED meteorites (Zolensky et al., 1996).

The endogenic part of the terrestrial analog is hypersthene. Hypersthene is a Ca-poor pyroxene (like the pyroxenes on Vesta and in HEDs, e.g., De Sanctis, Ammannito, et al., 2012; McCord et al., 1970; Mittlefehldt, 2015; and references therein) and was readily available in the quantities needed. The terrestrial sample names consist of the letter "H" for hypersthene, two digits for hypersthene's weight percentage, the letter "P" for Phobos Simulant and two more digits for the simulant's weight percentage.

The endogenic portion of the meteoritic regolith analogs was HED meteorites. The used meteorites are NWA 5748, NWA 5230, NWA 3359, and JaH 626. These meteorites were provided by the Westfälische Wilhelms-Universität Münster and had already been

sieved to different grain size fractions, like the terrestrial hypersthene. The HEDs were also used in the study by Ruesch et al. (2015) and are described in detail in that study. Here, the HEDs were mixed with Murchison, except NWA 3359 which was heated without adding an exogenic part, for comparative observations. A short summary of the mineralogy of the HEDs is given in the following, taken from the Meteoritical Bulletins #48, #90, #96, #100, #102 and Ruesch et al. (2015).

JaH 626 is a shocked eucrite comprising impact melt and polymict clasts of basaltic and cumulate eucrites. It contains pyroxene with augite exsolution lamellae and partly fine-grained recrystallization textures. Plagioclase partly occurs as fine anisotropic blades as a result from shock and quenching from melt. NWA 3359 is a polymict recrystallized eucrite showing clasts of basaltic eucrites and impact melt within a fine-grained clastic matrix; diogenite fragments occur. NWA 5230 is a heavily shocked polymict eucrite comprising basalt clasts and brecciated diogenite clasts within a fine-grained matrix. Impact melt clasts and droplets occur, and plagioclase was transformed to maskelynite due to shock. Pyroxene grains show augite exsolution lamellae. NWA 5748 is a howardite and contains eucrite and diogenite clasts and mineral fragments within a fine-grained matrix. Impact melt clasts and glassy spherules occur.

Due to the mentioned considerations about the abundance of CM2 material in the Vestan regolith presented in Reddy et al. (2012) and Michalik et al. (2021), we chose the exogenic, dark component of the regolith analogs to constitute 10–30 wt% of our mixtures. The Phobos Simulant was used with grain sizes from <25 to 63 µm to account for the generally small grain sizes of CM2 chondrites, whereas the Murchison sample also contained small amounts of larger grain sizes up to 250 µm. For the terrestrial hypersthene, the following proportions and grain size fractions were used: 40 wt% of 25–63 µm, 25 wt% of 63–125 µm, 15 wt% of 125–250 µm, and 5 wt% of 250–500 µm. The HED samples from the Westfälische Wilhelms-Universität Münster had different defined grain size fractions. They were mixed with the following average grain size proportions: 31.5 wt% of <45 µm, 36.5 wt% of 45–90 µm, 21.0 wt% of 90–250 µm, and 11.0 wt% of 250–500 µm.

Experimental and Measurement Procedure

The prepared samples were put in a small sample cup of about 1 cm in diameter, with a sample thickness of about 1–2 mm. They were heated to various temperatures and durations, listed in Table 2. Each aliquot of an unheated sample was only heated once. Not all samples were heated to the same temperatures and durations, due to the scarcity of sample material. Prior to heating,

TABLE 2. List of applied temperatures, durations, and if data of the second pyroxene absorption near 2.0 µm were acquired. Note that not all temperatures listed were applied for all listed durations.

Sample name	Temperature (°C)	Duration (h)	2.0 µm absorption
Hypersthene	400	72	No
Phobos Simulant	400	72	No
Murchison	400	72	Yes
NWA 3359	400	72	No
NWA 5748	400	72	Yes
NWA 5748M	200, 400, 600	2, 72	Yes
NWA 5230M	300, 400, 600	2, 72, 168	Yes
JaH 626M	200, 400, 600	2, 72, 168	No
H90P10	200, 400, 600	2, 72	Yes
H80P20	400	2, 72	Yes
H70P30	400	72	Yes

samples were stored in a dry cabinet for about 60 min, then sealed (to minimize air affecting the samples), and cooled down to approximately −80°C to roughly simulate starting conditions on Vesta. The samples were then removed from the container and placed into the vacuum chamber, where 0.1–0.01 mbar pressures were reached. Once near-vacuum was established, heating via an induction plate (from below) started. Average heating rates are about 3°C min^{-1} for low-temperature experiments and up to 12°C min^{-1} for higher temperatures. Once a constant temperature was applied for the desired amount of time, we let the samples cool down in vacuum before undertaking the reflectance measurements.

The reflectance measurements were acquired with a Bruker Vertex 80V Fourier Transform InfraRed (FT-IR) spectrometer that can obtain bidirectional spectra from the near UV (0.2 µm) to the far IR (up to 200 µm) (Maturilli et al., 2019). All samples were measured at an incidence angle of 30° and emission angle at 0° (phase angle = 30°) by means of a biconical Bruker A513 accessory. These are the same angles used to calibrate Dawn Framing Camera data (basis for observations of the PIDs). Thus, the resulting reflectance spectra will be similar to the observational data. All samples were measured at a spectral resolution of 4 cm^{-1} with 200 scans, yielding a high signal-to-noise ratio. The aperture for all measurements was 2 mm. We acquired every measurement twice or more times while rotating the sample for approximately 30°–120° in order to account for natural material differences. These differences were mostly very small with standard reflectance deviations of 0.003 for 70% of all samples, 0.005 for 90% of all samples, and 0.009 for 100% of the samples for the

resampled reflectance value at 0.750 µm (which ranges from 0.03 to 0.4). These multiple spectra were averaged to one representative spectrum of the respective sample which is displayed here.

The analyses presented in this work focus on the first pyroxene absorption band near 0.9 µm (band I); therefore, a VIS detector (Si-Diode) with a range from 0.4 to 1.1 µm was used. All measurements in this wavelength range were obtained using a tungsten lamp as light source and a CaF_2 beam splitter. For these measurements, a white Spectralon® standard was taken as reference. For a few samples, NIR spectra were acquired (1.0–16 µm) in order to characterize the second pyroxene absorption band near 1.9 µm (band II). These measurements were obtained using a Globar lamp as light source, a KBr beam splitter, an MCT detector (MCT = Mercury Cadmium Telluride), and an Infragold® standard as reference.

For most of the samples, it was not possible to measure the reflectance spectrum in vacuum as the samples contain hydrated phyllosilicates which are presumably responsible for "degassing events" while the samples are exposed to vacuum conditions within the measuring unit. Phyllosilicates contain water in their mineral structure and are prone to lose their volatiles when exposed to a sudden vacuum (velocity of air extraction could not be changed). This resulted in the dispersion of the sample within the measurement chamber, partly obscuring the mirrors. This in turn resulted in incorrect spectra which is why we chose to acquire the spectra at ambient pressure as air does not influence the pyroxene absorptions of interest. The spectra were corrected with a factor of 0.98 for the Spectralon® standard and with 0.8 for the Infragold® standard, as required by these standard references.

As mentioned earlier, we display spectra of heated surfaces and heated interiors of the samples. As it was not possible to systematically separate surface particles from interior particles very accurately, we measured the reflectance spectrum of the surface of each sample ("surface") and then manually mixed the surface and interior with a small spatula and measured their spectra afterwards. Thus, "interior" spectra also contain surface particles. This in turn means that sole interior particles probably show even larger differences with respect to the surface particles, which should be kept in mind.

In this study, we show whole reflectance spectra of the samples as well as the spectra resampled to FC band passes for spectral parameters, such as reflectance at 0.750 µm, band I strength (0.750/0.917 [µm]), band position (0.965/0.917 [µm]), and the visible slope (0.750/0.430 [µm]). Reflectance at 0.750 µm is used as an indicator of brightening or darkening. The 0.750/0.917 [µm] reflectance ratio is used as a measure of pyroxene band I strength. These two parameters are crucial to spectrally define the PIDs on Vesta, which is why we focus on those here as well. The 0.750/0.430 [µm] ratio is used as a measure of the formation and presence of hematite. The 0.965/0.917 [µm] ratio is used as a proxy measure of band I wavelength position to assess the spectrum-altering effects of hematite, as hematite has a 0.9 µm region absorption band at shorter wavelengths than pyroxene (e.g., Burns, 1993; Clark, 1999; Huguenin et al., 1977; Hunt, 1977; Morris et al., 1994).

Legends for whole spectra figures are ordered with the highest reflectance at 0.5 µm on top, where applicable. The presented values in Tables 3 and 4 match the data processing of Dawn FC data (Roatsch et al., 2013; Sierks et al., 2011), resampled to fit the respective filter responsivity functions in order to better compare the results with findings from Michalik et al. (2021).

For the NIR measurements at longer wavelengths, we extracted the reflectance values at 1.446 and 1.910 µm (the closest to the selected bands from the VIR analysis presented in Michalik, Stephan, et al., 2022) and calculated the pyroxene band II strength ratio 1.446/1.910 [µm]. Ratios are often used to eliminate systematic errors or effects of illumination conditions and topography.

Band depths would generally better be comparable when the continuum of a spectrum is removed, yet to enable the comparison with FC data, we refrain from removing continua here, also because the VIS detector measures the reflectance spectra only up to 1.1 µm, which is insufficient to define a continuum line.

Sample NWA 5748M has the most complete data set in terms of applied temperatures and durations. Other HED/CC-mixtures do not capture this wide range and serve as comparisons. Among the terrestrial samples, H90P10 has the most complete data set, while H80P20 and H70P30 were only heated to 400°C for 72 h.

Electron Probe Microanalysis

In order to understand the spectral changes observed during the experiments, we also analyzed the samples Murchison and NWA 5748M via electron probe microanalysis (EPMA). We use WDS (wavelength-dispersive spectroscopy) analysis as well as EDS (energy-dispersive spectrometer) analysis to evaluate mineral phases.

The samples were prepared as polished grain fragments embedded in epoxy. Due to the reddish character of the heated samples, we specifically searched for oxides, such as hematite (Fe_2O_3), which is a likely candidate and is known for its spectral reddening character. Thus, WDS analysis is presented as oxides.

TABLE 3. Absolute ("Δr") and relative ("%") changes of reflectance/reflectance ratios for heated samples. (Color table can be viewed at wileyonlinelibrary.com)

ID (Figure 4)	Sample name, T (°C), d (h)	Change type	0.750 µm	0.750/0.917 [µm]	0.965/0.917 [µm]	0.750/0.430 [µm]	1.446 µm	1.446/1.910 [µm]
1	NWA 5748M	Δr	−0.003	−0.038	−0.001	0.016		
	200, 2	%	−1.42	−2.74	−0.10	1.18		
2	NWA 5748M	Δr	0.006	0.025	0.003	0.111		
	200, 72	%	3.24	1.89	0.29	8.40		
3	NWA 5748M	Δr	0.003	0.005	−0.002	0.143		
	400, 2	%	1.60	0.37	−0.19	9.53		
4	NWA 5748M	Δr	0.008	0.020	0.003	0.123	0.019	0.032
	400, 72	%	4.12	1.51	0.29	8.06	10.98	2.66
5	NWA 5748M	Δr	0.042	0.078	0.001	0.362		
	600, 2	%	21.54	6.02	0.10	24.07		
6	NWA 5748M	Δr	0.025	0.121	0.007	0.297		
	600, 72	%	13.66	10.15	0.67	19.54		
7	NWA 5230M	Δr	0.005	−0.029	−0.003	0.179		
	400, 2	%	4.24	−1.98	−0.28	12.06		
8	NWA 5230M	Δr	0.001	−0.013	−0.001	0.204	0.003	0.029
	400, 72	%	0.81	−0.91	−0.09	13.58	2.54	2.41
9	NWA 5230M	Δr	0.027	−0.035	0.004	0.384		
	400, 168	%	21.77	−2.43	0.38	24.63		
10	NWA 5230M	Δr	0.021	0.091	−0.002	0.314		
	600, 2	%	18.26	6.62	−0.19	21.63		
11	NWA 5230M	Δr	0.037	0.020	−0.003	0.592		
	600, 72	%	30.58	1.45	−0.28	35.56		
12	JaH 626	Δr	0.029	0.049	−0.004	0.709		
	400, 168	%	20.57	4.03	−0.42	41.85		
13	JaH 626	Δr	0.047	0.083	−0.009	0.242		
	600, 72	%	42.73	7.09	−0.93	13.19		
	H90P10	Δr	−0.011	−0.042	−0.004	0.111		
	200, 2	%	−7.86	−3.08	−0.37	9.12		
	H90P10	Δr	−0.016	−0.048	−0.004	−0.030		
	200, 72	%	−11.11	−3.51	−0.36	−2.44		
14	H90P10	Δr	−0.018	−0.073	−0.016	−0.020	−0.007	−0.011
	400, 72	%	−12.95	−5.51	−1.46	−1.60	−5.74	−0.93
15	H90P10	Δr	−0.006	0.031	−0.003	0.090		
	600, 2	%	−5.45	2.55	−0.28	7.31		
16	H90P10	Δr	0.030	0.019	0.002	0.194		
	600, 72	%	28.30	1.53	0.18	14.34		
17	H80P20	Δr	−0.011	−0.041	−0.006	−0.016	−0.012	−0.069
	400, 72	%	−15.49	−3.49	−0.57	−1.31	−18.46	−6.20
18	H70P30	Δr	0.005	0.002	−0.003	0.002	0.006	−0.068
	400, 72	%	8.77	0.18	−0.29	0.18	11.54	−6.27
19	NWA 5748	Δr	−0.033	−0.070	−0.003	0.090	0.010	−0.001
	400, 72	%	−8.80	−4.03	−0.28	6.66	3.24	−0.07
	NWA 3359	Δr	−0.001	−0.038	−0.003	0.101		
	400, 72	%	−0.43	−2.24	−0.28	6.76		
	Hypersthene	Δr	−0.045	−0.092	0.001	0.188		
	400, 72	%	−18.52	−5.84	0.09	13.17		
	Murchison	Δr	0.019	n.a.[a]	n.a.	0.668	0.019	n.a.
	400, 72	%	28.79	n.a.	n.a.	34.33	22.89	n.a.
	Phobos Sim.	Δr	0.000	n.a.	n.a.	0.022		
	400, 72	%	0.00	n.a.	n.a.	2.12		

Note: IDs indicate numbering in Figure 4. Color code: light red for percentage values <0; green for percentage values >0.
Abbreviations: d, duration; T, temperature.

TABLE 4. Resampled spectral (ratio) values for all displayed materials. Resampling of spectra occurred according to the Dawn FC band passes.

Condition	T (°C) & d (h)	0.750 μm	0.750/0.917 [μm]	0.965/0.917 [μm]	0.750/0.430 [μm]	1.446 [μm]	1.446/1.910 [μm]
Hypersthene							
Unheated	–	0.269	1.724	1.152	1.493		
Surface	400, 72	0.243	1.574	1.155	1.427		
Interior	400, 72	0.198	1.482	1.156	1.615		
NWA 5748							
Unheated	–	0.373	1.770	1.064	1.320	0.304	1.521
Surface	400, 72	0.375	1.735	1.062	1.352	0.309	1.499
Interior	400, 72	0.342	1.665	1.059	1.442	0.319	1.498
NWA 3359							
Unheated	–	0.257	1.682	1.058	1.480		
Surface	400, 72	0.234	1.694	1.060	1.495		
Interior	400, 72	0.233	1.656	1.057	1.596		
Murchison							
Unheated	–	0.061	0.929	1.022	1.524	0.074	0.893
Surface	400, 72	0.066	0.898	1.031	1.946	0.083	0.853
Interior	400, 72	0.085	0.890	1.027	2.614	0.102	0.894
Phobos Simulant							
Unheated	–	0.035	1.029	0.995	1.023		
Surface	400, 72	0.027	0.970	1.011	1.036		
Interior	400, 72	0.027	0.953	1.016	1.058		
NWA 5748M							
Unheated	–	0.209	1.388	1.046	1.380	0.176	1.200
Surface	200, 2	0.212	1.386	1.048	1.354		
Interior	200, 2	0.209	1.348	1.047	1.370		
Surface	200, 72	0.185	1.324	1.046	1.321		
Interior	200, 72	0.191	1.349	1.049	1.432		
Surface	400, 2	0.188	1.357	1.047	1.500		
Interior	400, 2	0.191	1.362	1.045	1.643		
Surface	400, 72	0.194	1.328	1.049	1.526	0.173	1.201
Interior	400, 72	0.202	1.348	1.052	1.649	0.192	1.233
Surface	600, 2	0.195	1.296	1.048	1.504		
Interior	600, 2	0.237	1.374	1.049	1.866		
Surface	600, 72	0.183	1.192	1.048	1.520		
Interior	600, 72	0.208	1.313	1.055	1.817		
NWA 5230M							
Unheated	–	0.127	1.485	1.056	1.039	0.119	1.209
Interior	300, 2	0.133	1.508	1.057	1.616		
Interior	300, 72	0.143	1.452	1.060	1.610		
Surface	400, 2	0.118	1.468	1.064	1.484		
Interior	400, 2	0.123	1.439	1.061	1.663		
Surface	400, 72	0.123	1.425	1.066	1.502	0.118	1.204
Interior	400, 72	0.124	1.412	1.065	1.706	0.121	1.233
Surface	400, 168	0.124	1.441	1.062	1.559		
Interior	400, 168	0.151	1.406	1.066	1.943		
Surface	600, 2	0.115	1.375	1.067	1.452		
Interior	600, 2	0.136	1.466	1.065	1.766		
Surface	600, 72	0.121	1.378	1.071	1.665		
Interior	600, 72	0.158	1.398	1.068	2.257		
JaH 626M							
Unheated	–	0.149	1.337	0.943	1.411		
Interior	200, 2	0.150	1.309	0.945	1.581		
Interior	200, 72	0.117	1.300	0.949	1.436		

TABLE 4. *Continued.* Resampled spectral (ratio) values for all displayed materials. Resampling of spectra occurred according to the Dawn FC band passes.

Condition	T (°C) & d (h)	0.750 μm	0.750/0.917 [μm]	0.965/0.917 [μm]	0.750/0.430 [μm]	1.446 [μm]	1.446/1.910 [μm]
Surface	400, 168	0.141	1.215	0.958	1.694		
Interior	400, 168	0.170	1.264	0.954	2.403		
Interior	600, 2	0.168	1.256	0.951	2.358		
Surface	600, 72	0.110	1.170	0.966	1.835		
Interior	600, 72	0.157	1.253	0.957	2.077		
H90P10							
Unheated	–	0.135	1.373	1.094	1.255	0.124	1.228
Surface	200, 2	0.140	1.362	1.094	1.217		
Interior	200, 2	0.129	1.320	1.090	1.328		
Surface	200, 72	0.144	1.369	1.096	1.232		
Interior	200, 72	0.128	1.321	1.092	1.202		
Interior	400, 2	0.107	1.268	1.077	1.257		
Surface	400, 72	0.139	1.324	1.095	1.252	0.122	1.178
Interior	400, 72	0.121	1.251	1.079	1.232	0.115	1.167
Surface	600, 2	0.110	1.214	1.090	1.232		
Interior	600, 2	0.104	1.245	1.087	1.322		
Surface	600, 72	0.106	1.240	1.094	1.353		
Interior	600, 72	0.136	1.259	1.096	1.547	0.132	1.146
H80P20							
Unheated	–	0.080	1.248	1.062	1.100	0.069	1.153
Interior	400, 2	0.084	1.246	1.060	1.186		
Interior	400, 72	0.071	1.174	1.060	1.220	0.065	1.113
Surface	400, 72	0.060	1.133	1.054	1.204	0.053	1.044
H70P30							
Unheated	–	0.068	1.176	1.049	1.050	0.062	1.136
Interior	400, 72	0.057	1.129	1.046	1.090	0.052	1.084
Surface	400, 72	0.062	1.131	1.043	1.092	0.058	1.016

Abbreviations: *d*, duration; *T*, temperature.

Analyzed species were SiO_2 (Standard Cr-Augite, NMNH 1649C, TAP crystal), TiO_2 (Standard Ilmenite, USNM 96189, PETJ crystal), Cr_2O_3 (Standard Chromite, USNM 11707, LIFH crystal), FeO (Standard Magnetite, USNM 11488, LIFH crystal), MnO (Standard Ilmenite, USNM 96189, PETJ crystal). The applied voltage was 15 kV with a current of 15 nA and a focused beam. The ratio of the molecular weights of hematite and the measured FeO is 1.1113, so this factor is applied to the FeO results. Images are displayed in BSE (backscattered electrons) mode, which is sensitive to the atomic number of the elements. In this mode, hematite shows a higher signal (i.e., brighter) than for example olivine or pyroxene.

OBSERVATIONS

VNIR Reflectance

Our results are shown in two separated parts. Key observations are presented in the following, while a detailed description of all VNIR reflectance observations, including a display of all obtained spectra, is shown in the Appendix.

With respect to the unheated sample, none of the heated samples showed both higher reflectance and pyroxene band I strength after heating, except sample NWA 5230M heated to 300°C for 2 h (this is one out of 32 heating experiments). All other samples and temperature/duration varieties show inconsistent results with respect to their unheated counterpart (e.g., higher reflectance but lower pyroxene band I strength, or vice versa, or both lowered).

When comparing spectra of samples heated to different temperatures, the only sample yielding both higher reflectance and pyroxene band I strength for a reasonable situation comparable to Vesta (higher temperature and/or longer duration) is for H90P10 after 600°C, 72 h with respect to H90P10 after 600°C, 2 h. Interestingly, for JaH 626M and NWA 5748M, the 600°C, 2 h aliquot yielded higher reflectance and pyroxene band I strength than the 600°C, 72 h aliquot, which is counterintuitive to the situation on Vesta (the less voluminous surrounding deposit would
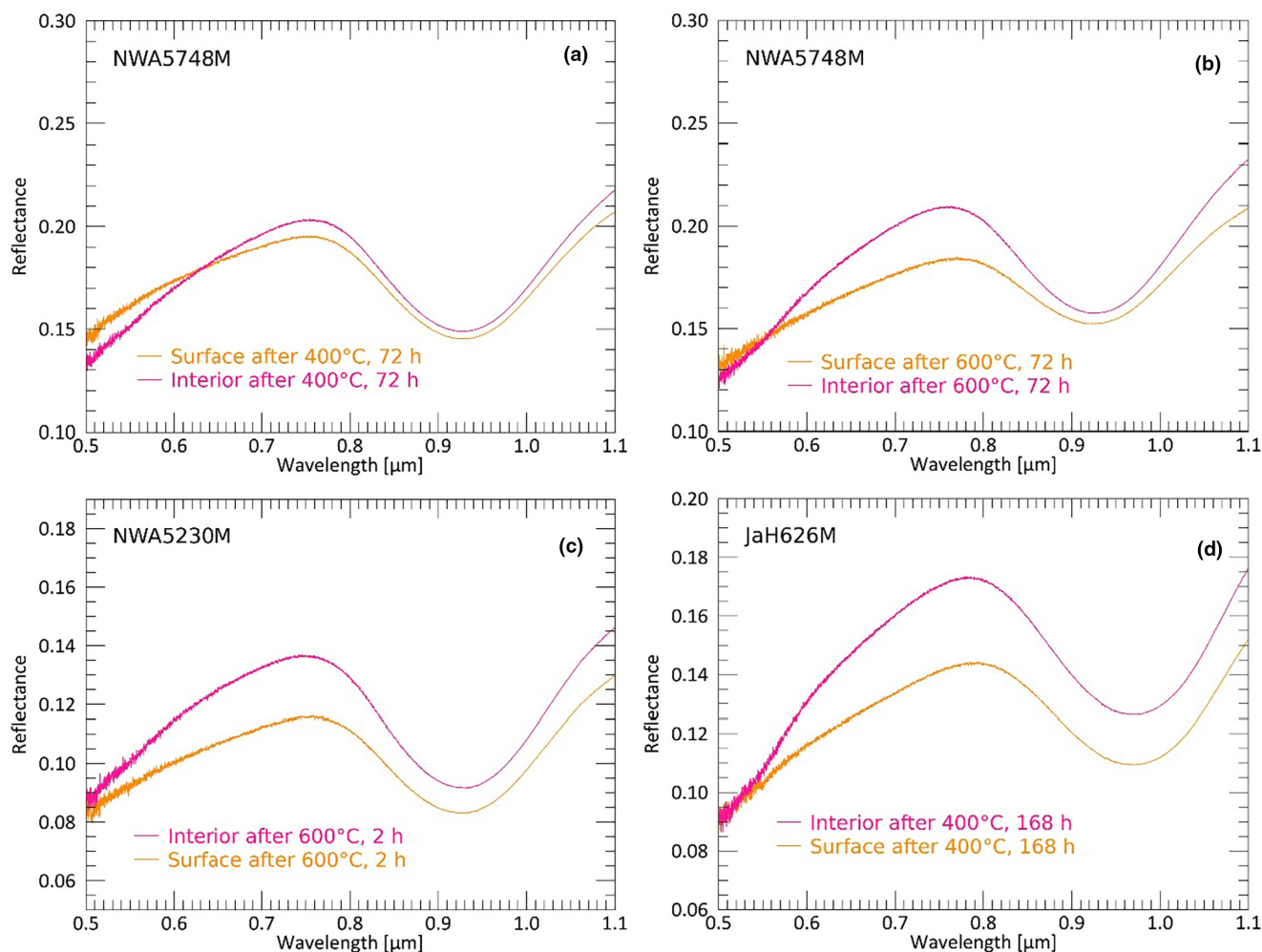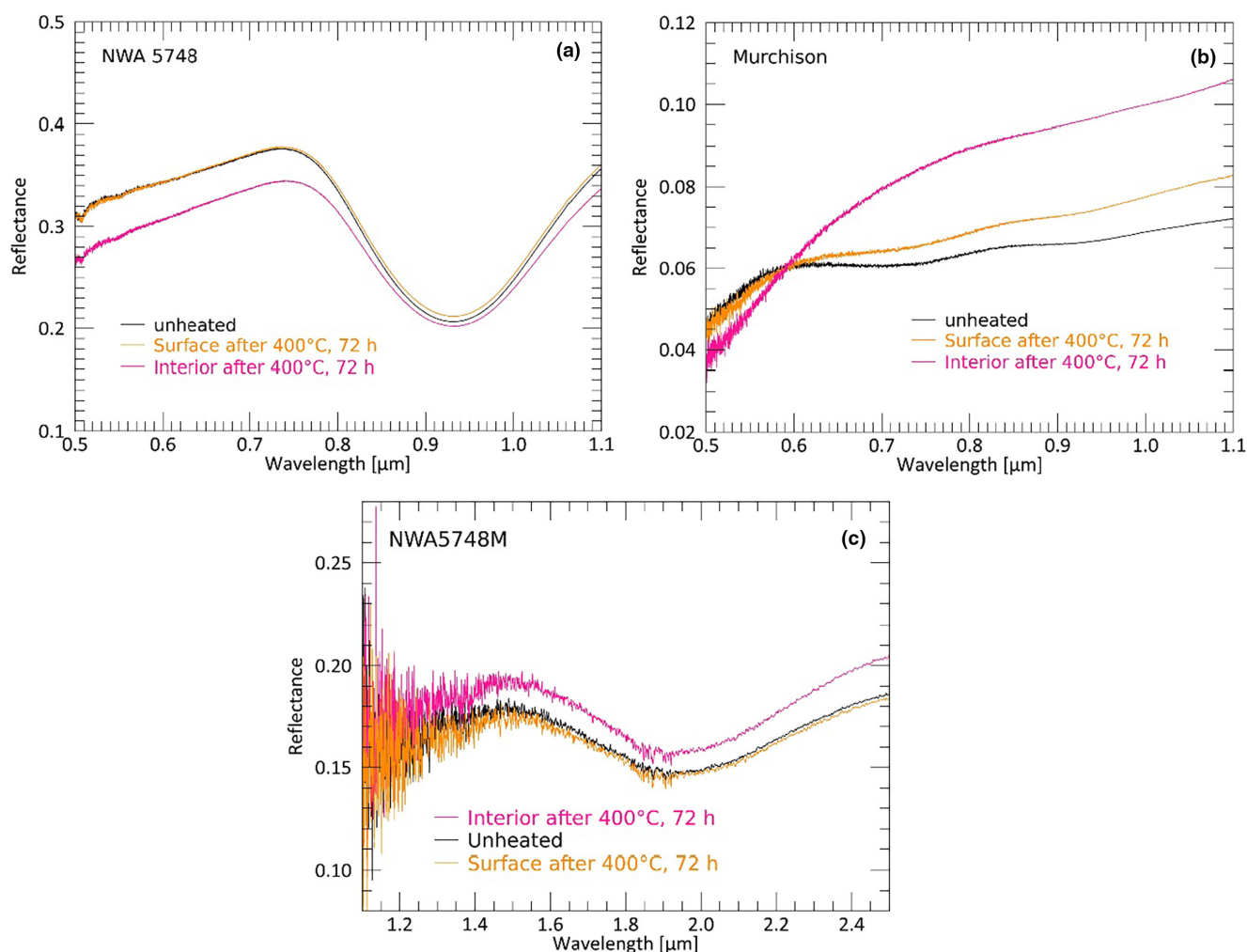
FIGURE 2. Wavelength versus reflectance of heated surfaces and interiors of samples: (a) NWA 5748M after 400°C, 72 h, (b) NWA 5748M after 600°C, 72 h, (c) NWA 5230M after 600°C, 2 h, and (d) JaH 626M after 400°C, 168 h. Legend entries are ordered after reflectance at 0.5 μm, orange spectra are surface spectra, and pink spectra are interior spectra. (Color figure can be viewed at wileyonlinelibrary.com)

not be able to maintain a given temperature for longer durations).

In contrast, when comparing the surface of a heated sample with its interior, many samples show a similar behavior to PIDs: Many interiors of especially the meteoritic analogs show both higher overall reflectances and pyroxene band I strengths with respect to their surfaces. This is surprising as sample containers were filled with material only to about 1–2 mm height.

Figure 2 shows example spectra of the surface and interior of heated samples NWA 5748M (Figure 2a,b), NWA 5230M (Figure 2c) and JaH 626M (Figure 2d). NWA 5748M is shown for different temperatures to highlight the large variations that different temperatures can cause.

Each sample appeared to show a different "onset" temperature for the process(es) causing the most prominent changes: higher visible slopes, higher reflectances, and higher pyroxene band I strengths. For example, the interior of sample NWA 5748M already develops higher reflectance and pyroxene band I strength than its surface at 200°C when heated for 72 h, whereas NWA 5230M shows these two characteristics develop only at 600°C (see Tables 3 and 4 and Figure 4b). Moreover, at 600°C, the interior of NWA 5230M shows a stronger increase in pyroxene band I strength when heated for 2 h, in contrast to 72 h, whereas for NWA 5748M, pyroxene band I strength increases stronger when heated for 72 h, instead of 2 h (see Table 3). Increases in visible slopes represent the most consistent change among all temperatures and durations, and developed for every heating experiment of meteoritic analog mixtures (Tables 3 and 4 and Figure 4c).

Table 3 quantifies the changes of each spectral parameter for each sample where separated surface/interior data are available. It illustrates negative relative changes in red cell color, and positive relative changes in green cell

FIGURE 3. Wavelength versus reflectance of heated surfaces and interiors of samples: (a) NWA 5748 after 400°C, 72 h; (b) Murchison after 400°C, 72 h; and (c) NWA 5748M after 400°C, 72 h (band II). Legend entries are ordered after reflectance at 0.5 and 1.5 μm, respectively. Orange spectra are surface spectra, pink spectra are interior spectra, black spectra are unheated spectra of the original sample. (Color figure can be viewed at wileyonlinelibrary.com)

color. Both reflectance at 0.750 μm and pyroxene band I strength increase especially for the meteoritic analogs, although it must be noted that the data set for the terrestrial analogs is more limited.

Heating pyroxene-bearing endmember material shows very different results. The interiors of NWA 5748 (Figure 3a), NWA 3359, and terrestrial hypersthene all show a decrease of reflectance and pyroxene band I strength (Tables 3 and 4) for their interior versus surface, strongly implying that the addition of volatile-bearing material is causing the higher reflectances and band I strengths of interiors.

Terrestrial analogs generally show a weaker extent of spectral changes upon heating. H90P10 only shows both increasing reflectance and pyroxene band I strength for its interior when heated to 600°C for 72 h (Table 3 and

Figure A1.5e). H70P30, which contains 20 wt% more volatile-bearing material, shows this behavior at 400°C, 72 h (Table 3 and Figure A1.6d), again implying that the abundance of volatile material plays a key role.

Heating of the volatile-bearing endmembers to 400°C for 72 h also produces varying results. The reflectance of the Phobos Simulant is decreasing, both for its surface and interior with respect to its unheated aliquot (Table 3 and Figure A1.7e), while its interior shows slightly higher visible slopes than its surface. In contrast, for Murchison, both the reflectance of the surface yet more strongly of the interior increase significantly (Figure 3b).

Limited data are available for the pyroxene absorption band II near 1.9 μm. However, for samples NWA 5748M and NWA 5230M heated to 400°C for 72 h, both higher reflectance and higher pyroxene

absorption strength of the interior continue in the near infrared (Tables 3 and 4, Figures 3c, 4a and A1.8b). This is not the case if sample NWA 5748 is not mixed with Murchison (Tables 3 and 4, Figures 4a and A1.8c).

Figure 4 illustrates the relationship of the spectral parameters given in Tables 3 and 4 for the interiors and surfaces of the different samples. Three pairs of terrestrial analogs are shown while the other terrestrial data were omitted for the benefit of more clarity. Data of meteoritic analogs are shown in yellow/red circles, terrestrial data in blue/green diamonds. Arrows are connecting a sample's surface with its interior and each arrow represents one heating experiment; numbering is according to Table 3. The subsequent Table 4 reports all obtained values for each parameter. It is worth noting that the differences between surface and interior increase with temperature and duration, yet the overall level of absolute values decreases, which is why an aliquot heated to 600°C, 72 h

(interior) still exhibits lower pyroxene band I strength than for example an aliquot heated to 400°C, independent of the duration or interior/surface condition.

All panels in Figure 4 show that spectral changes of meteoritic samples are generally more pronounced, and that the changes of terrestrial material are mostly negative (see also Table 3). In general, changes are more pronounced with increasing temperature and partly also with duration. Band position changes (panel 4d) are inconsistent with temperatures/duration systematics and appear random. In addition, the extent of band position changes is very small. When comparing pyroxene band I versus band II strength (panel 4a), available data show that for sample NWA 5748M (#4), both pyroxene absorptions increase for their interior versus surface spectra. In contrast, absorption strengths decrease when NWA 5748 is not mixed with Murchison (#19). Figure 4c illustrates that the visible slope increases for all meteoritic
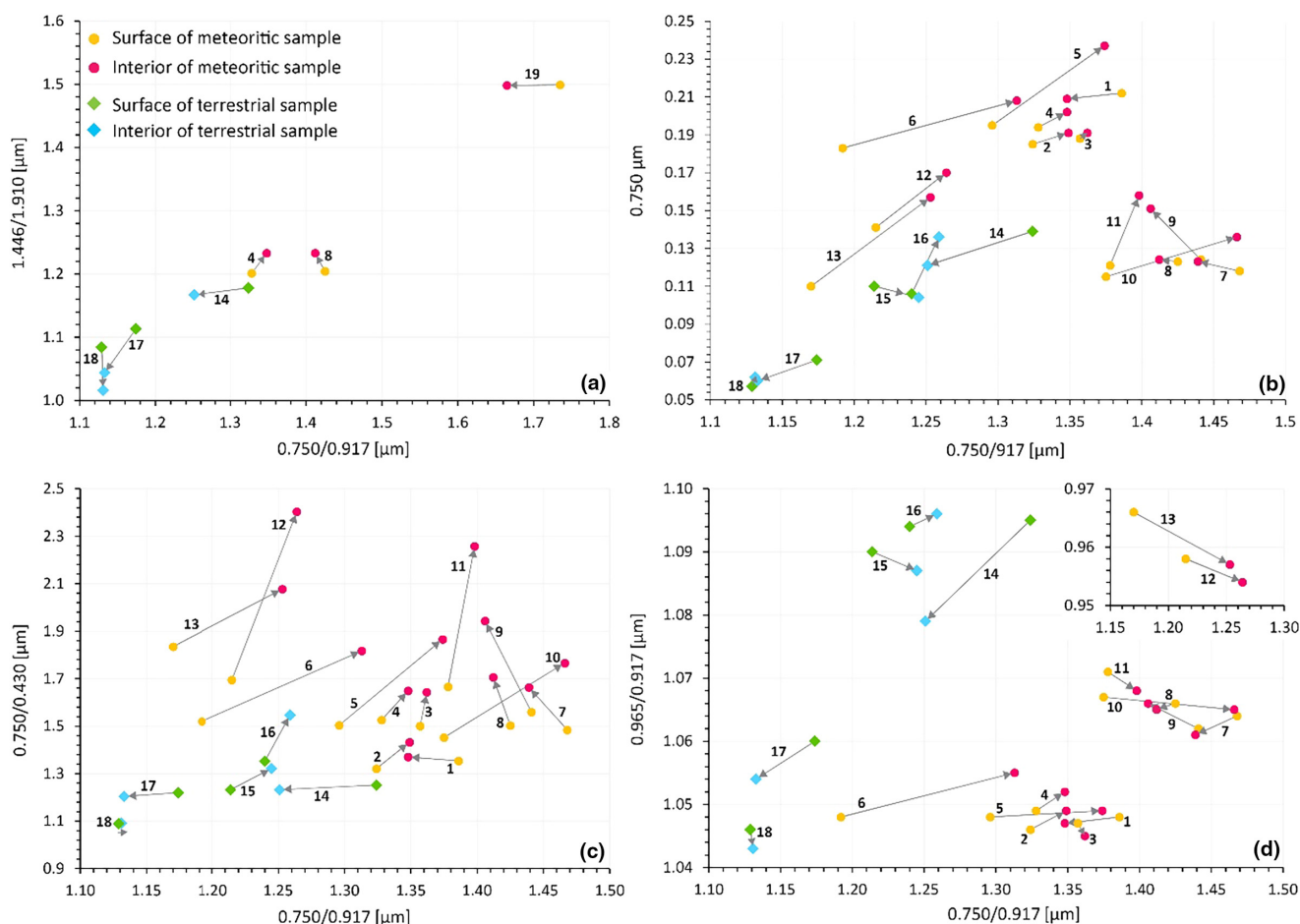
FIGURE 4. (a) 0.750/0.917 [μm] versus 1.446/1.910 [μm] (indicator for band I versus band II strength), (b) 0.750/0.917 [μm] versus 750 μm (most important parameters to compare with PIDs on Vesta), (c) 0.750/0.917 [μm] versus 0.750/0.430 [μm] (band I strength versus visible slope), and (d) 0.750/0.917 [μm] versus 0.965/0.917 [μm] (band I strength versus band position). Meteoritic samples are shown in circles, terrestrial samples in diamonds. Arrows connect the surface of a heated sample data point to its interior data point. Sample numbering is according to ID in Table 3. (Color figure can be viewed at wileyonlinelibrary.com)

interiors, also when pyroxene band I strength does not (#1, #7, #8, #9). Figure 4b moreover shows that all meteoritic interiors increase in reflectance (except #1, NWA 5748M 200°C, 2 h) while terrestrial interiors decrease in reflectance; except the two samples (#16 & #18) where both reflectance and pyroxene band I strength increase for interiors versus surfaces.

EPMA

Here, we present EPMA results of Murchison and NWA 5748M. As seen in Figure 3, Murchison is the only endmember experiencing significant reddening after heating to 400°C for 72 h which is likely the cause for the spectral changes of the meteoritic regolith analogs, as well. NWA 5748M is, in this study, the meteoritic analog with the largest data set and a clear systematic increase in visible slope, reflectance, and pyroxene band I strength (the latter two only with respect to its heated surface). The unheated as well as 600°C, 72 h aliquots were chosen for EPMA due to the most pronounced development of these spectral characteristics upon heating. Due to the strong reddening of the heated samples, we specifically looked out for iron oxides, that is, hematite, as its formation during the heating process is the most likely cause for this reddening. Several spots that showed the presence of iron oxides with the EDS were analyzed via WDS in order to evaluate the species (hematite/ magnetite). All selected locations had values typical for hematite (below 90 wt% FeO). The according Fe_2O_3 wt % of the numbered locations within the BSE (backscattered electrons) images shown in the following is given in Table 5. Other very minor oxide constituents were found to be SiO_2 and Cr_2O_3 (see Appendix Table A2.1).

Hematite was only identified within the heated aliquots of Murchison and NWA 5748M. It often occurs as "coatings" or rims around sulfide or metal grains, but also occurs around pyroxene grains. Figure 5 displays exemplary single grains found in NWA 5748M, depicting hematite coatings around various grains. Inclusions of iron metal within pyroxene host grains did not appear to transform or build a hematite coating (example in Figure 5a, upper left). Figure 6 shows BSE images of the

heated aliquot of Murchison, depicting an accumulation of hematite droplets within a larger grain of likely phyllosilicates and partly olivine. Although sulfides, metal and pyroxene grains also exist in the unheated aliquots of both samples, hematite was not observed (Figure 7).

The Fe_2O_3 values do not always add up to 100% and can be affected by various effects: (1) Hematite phases were often quite narrow, possibly not covering the whole measurement spot size; (2) hematite phases also exhibited small inhomogeneities, inclusions and pores, possibly also affecting the WDS result; and (3) the samples were prepared as polished grains embedded in epoxy. As the available grains possess very different properties regarding their hardness and constitution, a homogenous polish of all grains could not be achieved.

DISCUSSION

The results of the presented heating experiments clearly show that exposing the given regolith analogs to elevated temperatures can significantly change their spectral characteristics. However, these changes do not appear to be entirely systematic, neither within a given sample suite nor within a whole suite (meteoritic/ terrestrial) or across the studied temperature range. The causes behind the observed spectral changes are discussed in the following. As mentioned, we focus on spectral parameters that would be most useful for comparison to the PIDs and to understand their formation conditions: 0.750 μm reflectance, 0.750/0.917 and 0.750/0.428 [μm] reflectance ratios.

The Different Roles of Volatile-Bearing and Pyroxene-Dominated Material and their Relationship

Heating (400°C, 72 h) of the utilized volatile-bearing and pyroxene-dominated endmembers mostly results in a decrease of overall reflectance and pyroxene band I strength (for pyroxene-bearing endmembers), except for Murchison (Figure 3b). The reflectance spectrum of the heated Murchison aliquot exhibits a significantly steeper visible slope and an increased overall reflectance beyond ~0.6 μm. The Phobos Simulant, which is supposed to represent a CC analog, does not experience similar effects at this temperature. However, we suggest that a related mechanism occurs near 600°C, where we see similar significant changes in the H90P10 sample. These observations indicate that the individual species of chondritic material appears to play a crucial role when considering the available temperatures in the ejecta blanket. As we see with sample NWA 5748M, even at a relatively low temperature of 200°C, both

Table 5. WDS analysis for Fe_2O_3 (hematite) of the numbered locations in Figures 5 and 6.

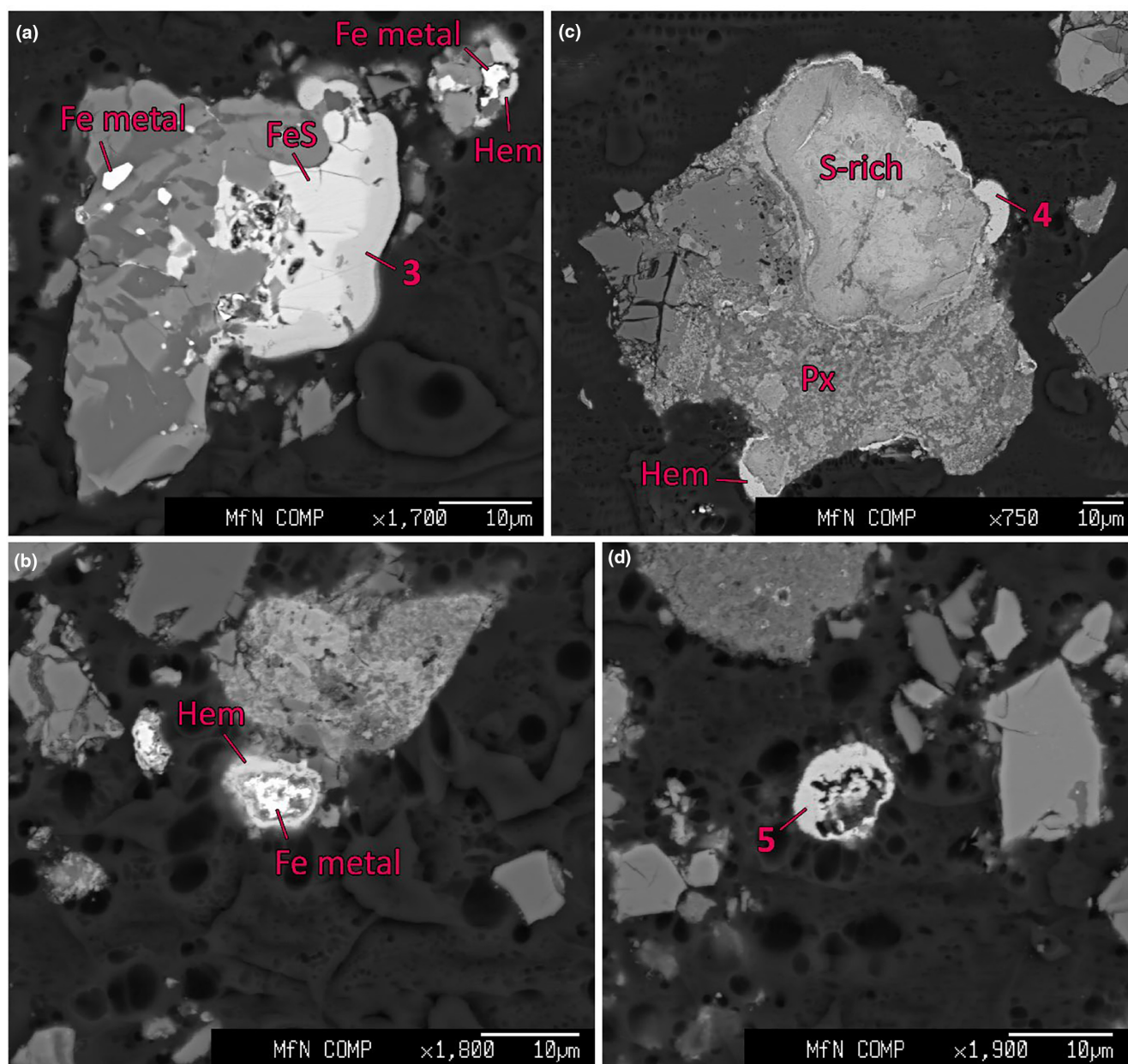| Location	Fe_2O_3 wt%
1	99.97
2	98.90
3	98.52
4	92.45
5	95.86

FIGURE 5. BSE images of NWA 5748M, heated to 600°C for 72 h. (a) Grain with hematite coating (location 3) over iron sulfide phase. Larger grain also includes metallic iron that has not been transformed. Nearby small grain (upper right) shows hematite rims to iron metal. (b) Hematite rim around iron metal. (c) Hematite coating around sulfur-rich phase (upper right) and pyroxene (bottom). The sulfur-rich phase could not be identified and a corresponding EDS spectrum is given in Appendix (Figure A2.2). (d) Hematite phase not attached to another grain. *Fe*, iron; *Hem*, hematite; *Px*, pyroxene; *S*, sulfur. (Color figure can be viewed at wileyonlinelibrary.com)

higher reflectance and pyroxene band I strength can form. In addition, the individual meteorite properties might also play a role, which was not examined in this study. Even when meteoritic samples are from the same taxonomic group, they will have mineralogical variabilities that likely affect reaction mechanisms. For instance, NWA 5748 contains impact melt which would be more reactive than crystalline phases. NWA 5320 contains maskelynite (amorphous plagioclase), which would also be more reactive than crystalline phases. Thus, comparisons between samples must be undertaken carefully. As alteration processes should be more advanced with increasing durations, the contradicting behaviors of NWA 5748M and NWA 5230M heated to 600°C for different durations probably emphasize these different mineralogical
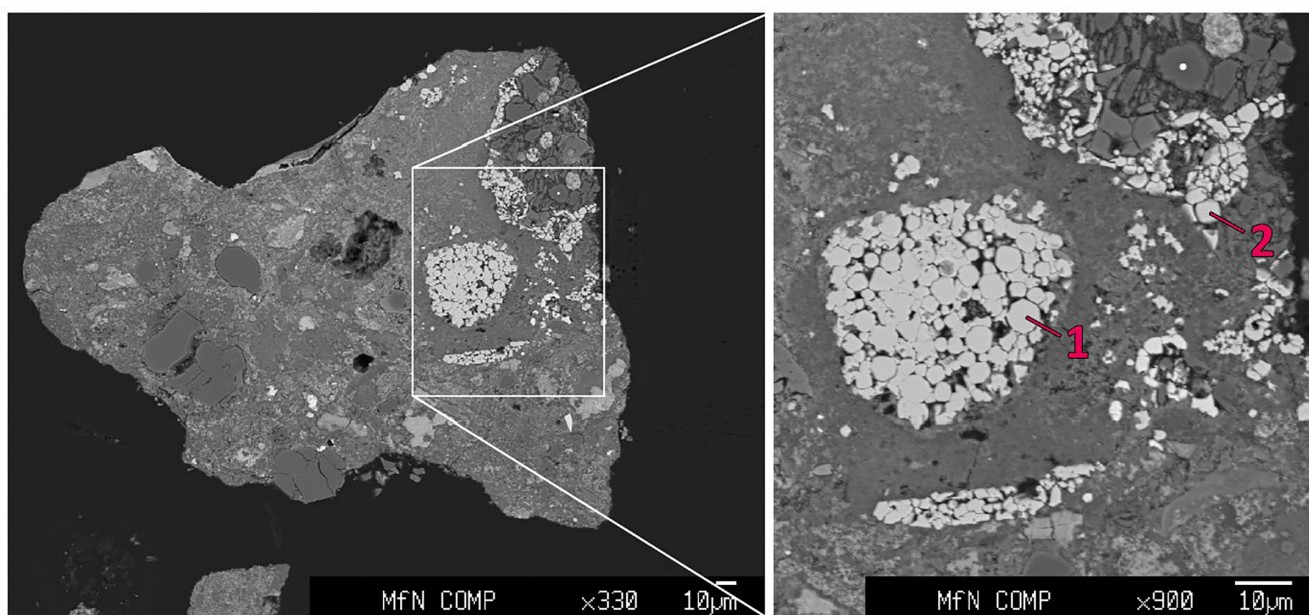
FIGURE 6. BSE image of a grain from Murchison heated to 400°C, 72 h. The enlargement image depicts the locations of WDS analysis shown in Table 5. (Color figure can be viewed at wileyonlinelibrary.com)

variabilities. In addition, HED material is likely more reduced than the utilized terrestrial hypersthene, possibly facilitating reactions with volatiles.

For the terrestrial sample H70P30 with a higher CC analog content, this effect appears to start already at 400°C, which indicates that a higher CC content in these analog samples facilitates the onset of the alteration process. This is also observed in the meteoritic suite, where NWA 5748M with 20 wt% Murchison starts to show significant changes at lower temperatures (at 200°C, 72 h) than NWA 5230M (at 600°C) with 15 wt% Murchison. If the abundance of volatile-bearing material correlates with a facilitated onset of processes creating the observed spectral changes, it might also correlate with a facilitated onset of PID formation. This in turn could explain why PIDs occurring in ejecta units with higher overall OH contents also occur at sites where no prominent pre-existing craters or ridges are readily identifiable and/or present (Michalik et al., 2021).

The remarkable change of the Murchison reflectance spectrum is not in accordance with observations by Cloutis et al. (2012), who show the absolute reflectance in the VIS and NIR range of heated Murchison. Their data for Murchison were initially presented by Hiroi et al. (1993, 1994), who heated their samples for 1 week in a low-pressure hydrogen atmosphere. This is a different heating procedure from the one presented here and therefore likely produces different results. The heating of Murchison was also performed in other studies (not focusing on spectral characteristics) (e.g., Yamashita et al., 2015; Zolensky et al., 1994), which report on the

decomposition of tochilinite, a hydroxysulfide mineral and major constituent of the Murchison matrix. Tochilinite is a brown to black mineral, thus darkening an overall spectrum. The loss of tochilinite would increase the overall reflectance and pyroxene band strength; however, this would also be true for material devoid of CC material and create similar spectral properties as "bright" material on Vesta (which is not the case), as discussed already in Michalik et al. (2021). However, heating of carbonaceous chondrites leads to more complex spectral changes, as different phases are transformed at different temperatures (e.g., Hiroi et al., 1994; Sidhu et al., 2023; Zolensky et al., 1994). These changes include a decrease in the 0.7 μm region Fe^{3+}-Fe^{2+} charge transfer band (Sidhu et al., 2023) and both increases and decreases in reflectance. Thus, spectra of heated CC-bearing material on Vesta (where dark compounds have been lost/decomposed) might still show different spectral characteristics than the bright material devoid of CC material.

Few studies exist on the heating of HED material (e.g., Hinrichs & Lucey, 2002; Miyamoto & Mikouchi, 2001). These studies reported that the spectra of heated HED samples generally do not change significantly but tend to lose spectral contrast and pyroxene band strength after heating, which is identical to what is observed in this work for the HEDs NWA 3359 and NWA 5748 and the terrestrial hypersthene. Hinrichs and Lucey (2002) observed a shift of band minima to longer wavelengths, though they measured the sample during the heating process at the elevated temperatures. These studies
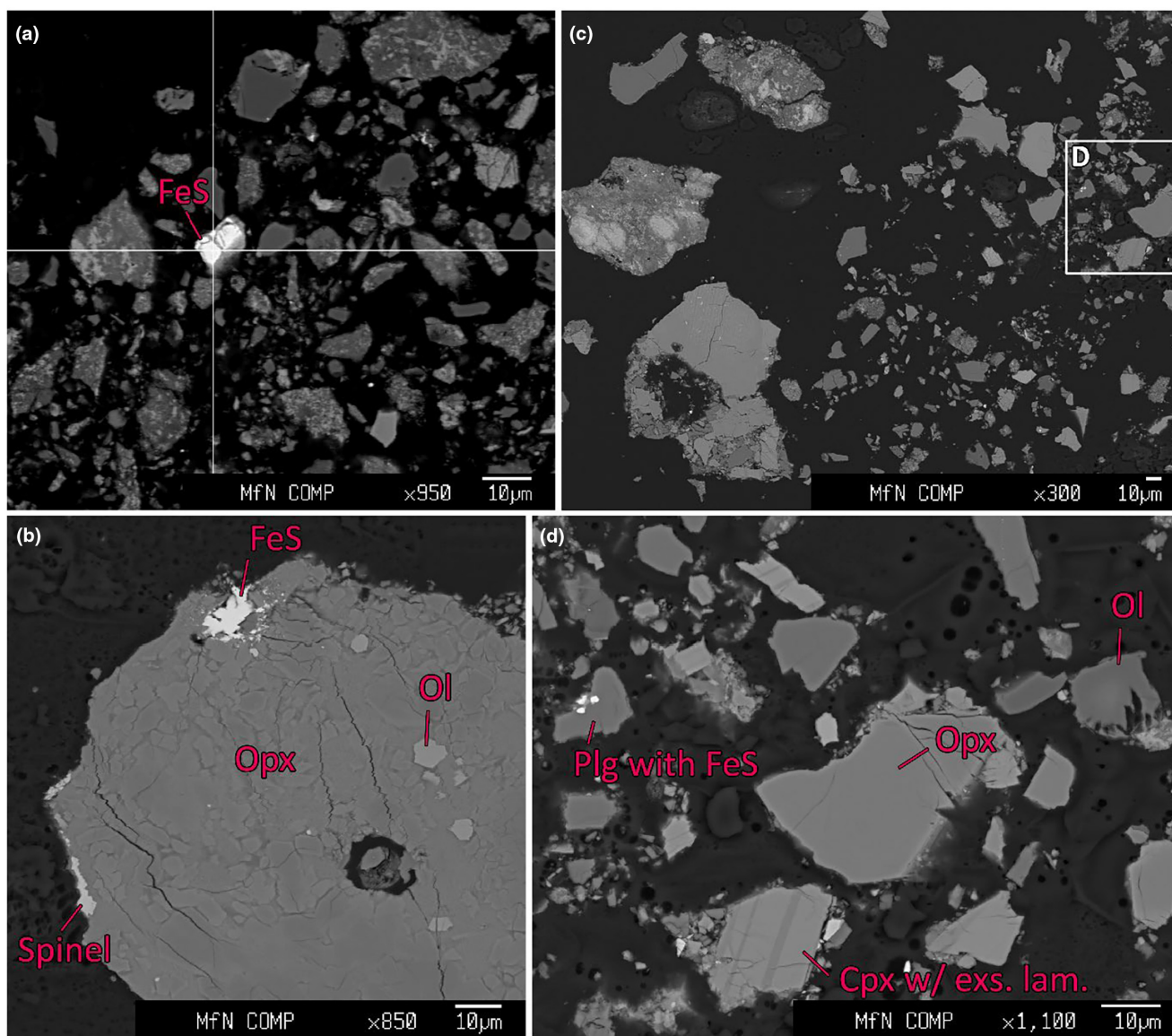
FIGURE 7. (a) BSE image of a grain from unheated Murchison, depicting a bright iron sulfide in the center. (b) BSE image of a grain from unheated NWA 5748M depicting a pyroxene grain with olivine inclusions as well as iron sulfide and spinel as additional phases. No hematite observable. (c, d) BSE images of multiple grains from unheated NWA 5748M with no signs of hematite coatings or rims. (d) Shows typical howarditic compositions with orthopyroxenes and clinopyroxenes including Ca-rich exsolution lamellae as well as olivine and plagioclase showing inclusions of iron sulfide. *Cpx*, clinopyroxene; *exs. lam.*, exsolution lamellae; *Ol*, olivine; *Opx*, orthopyroxene; *Plg*, plagioclase. (Color figure can be viewed at wileyonlinelibrary.com)

emphasize that the addition of volatile-bearing material is crucial for the observed spectral changes to occur in the first place.

Development of an Increased Visible Slope and the Formation of Hematite

After heating, nearly all samples showed an increase of the visible slope, both for interiors versus surfaces but also for interiors versus unheated samples.

For the example spectra shown for one PID in Figure 1 (taken from Michalik et al., 2021), the visible slope of the depicted PID is slightly larger than that of its surrounding (1.232 vs. 1.179), although systematic observations of the PIDs' visible slopes were not included in their work. Our results show a larger increase of visible slopes with higher temperatures, possibly indicating that the ejecta deposits experienced temperatures below 400°C. However, many parameters can influence this. For example, the terrestrial analogs

that show higher reflectance and pyroxene band I strengths for the interior versus surface exhibit more moderate visible slope increases. This indicates again that different chondritic species might be affecting the development of higher visible slopes in different ways. Moreover, our samples are heated from below, which is different to the situation on Vesta. This could lead to varying alteration conditions, such as release of volatiles only from the base of the sample which could react with the surrounding sample as they diffuse out of the sample. Reaction types and intensities could be affected by the rate, duration, and temperature of heating from below.

The most likely explanation for the reddening of laboratory samples is the formation of ferric iron compounds, that is, hematite. Microscopic observations have shown that very small red phases (<10 to 100 μm) are present in the heated sample NWA 5748M (600°C, 72 h), scattered throughout grains, and attached to grains. In contrast, the unheated sample NWA 5748M did not show such red phases. EPMA confirmed the presence of hematite, seen as hematite coatings formed around iron sulfide, iron metal, and pyroxene grains. The development of hematite can explain the strong reddening of the laboratory heated samples and implies an oxidation process. However, we do not observe the typical hematite absorption features at 0.66 and 0.85 μm (e.g., Morris et al., 1985), which might be masked by the spectral predominance of pyroxene or might be absent due to poor crystallinity of the hematite (EPMA images show roundish, amorph-like shapes of the found hematite, see Figure 5) or due to insufficient abundances. However, some samples shown in this study might indicate the development of another typical absorption at around 0.5 μm (e.g., Morris et al., 1985), indicated by a prominent kink or sudden near-VIS reflectance loss of spectra of relatively high-temperature interior aliquots (e.g., Figure 2d) at about 0.6 μm toward shorter wavelengths. It should be noted that the absorption coefficient of hematite can vary by orders of magnitude over the visible spectral region (e.g., Zhang et al., 2015); leading to a steep spectral slope as hematite dominates this wavelength region, and its spectrum-altering effects gradually wane toward longer wavelengths.

The development of hematite during oxidation/heating is a commonly observed process and has also been observed for extraterrestrial materials. Dixit et al. (2021) showed that hematite develops after heating several ordinary chondrites in air (600°C was the lowest of the studied temperatures). It is moreover well known for Mars and SNC meteorites that (nanophase) hematite is a common Martian weathering product (e.g., Minitti et al., 2002; Morris et al., 1989, 2000). Morris et al. (1994) showed that relatively unoxidized pyroxene-bearing impact melt samples from the terrestrial crater Manicouagan (Quebec, Canada) develop hematite when heated and oxidized. This oxidation occurs subsolidus and the spectra gradually change from well-pronounced pyroxene spectra to essentially hematite spectra at 1000°C. At 400 and 500°C, the spectra are already significantly reddened (Morris et al., 1994) but still exhibit distinct pyroxene absorptions, very similar to the results shown here (yet they do not indicate higher reflectance or band strength).

Furthermore, the development of hematite was observed while simultaneously oxidizing and heating various pyroxenes (600°C in air, Cutler et al., 2020) to infer Venus surface alteration. Straub et al. (1991) also observed the formation of nanophase hematite when heating pyroxenes in air. Li et al. (2020) moreover presented evidence for the presence of hematite on the Moon. The Moon's surface is highly reduced and shows only up to 1 wt% of ferric iron (Li et al., 2020). Some pixels of Moon Mineralogy Mapper spectra suggesting the presence of hematite shows significantly shallower visible slopes than those of pure hematite, possibly resulting from exposure to the space environment, or differences in particle size and abundance (Li et al., 2020). However, no studies exist on the space weathering of hematite, which the authors likewise point out. EPMA results presented here show that hematite forms as very thin coatings (about ≤2 μm), so these coatings might be prone to weathering of any kind.

Increase of Reflectance and Intensification of Pyroxene Band Strength

Even if hematite was proven to exist on Vesta (or any other iron (hydr-)oxide), it cannot explain the intensification of pyroxene absorptions, which affects both pyroxene crystal field transitions in the near infrared and was observed for PIDs on Vesta (Michalik et al., 2021; Michalik, Stephan, et al., 2022) as well as in this study. Hematite is generally darker than pyroxene in the VIS range and lowers band strengths and reflectance of pyroxene (Figure 8) as it absorbs more light and can scatter it before it encounters the pyroxene grain. Data of powdered pyroxene and hematite mixtures strengthen this concept, which is illustrated in Figure 8. The nanophase hematite reduces pyroxene band strength of both pyroxene absorptions at 0.9 and 1.9 μm, lowers the reflectance below ~0.8 μm yet increases reflectance of the mixtures beyond ~0.8 μm. Moreover, the band position moves toward shorter wavelengths with increasing hematite proportions in the mixture. This is likely due to the overlapping of the shallower hematite absorption band near 0.86 μm. However, no heating was involved in acquiring the data shown in Figure 8. In
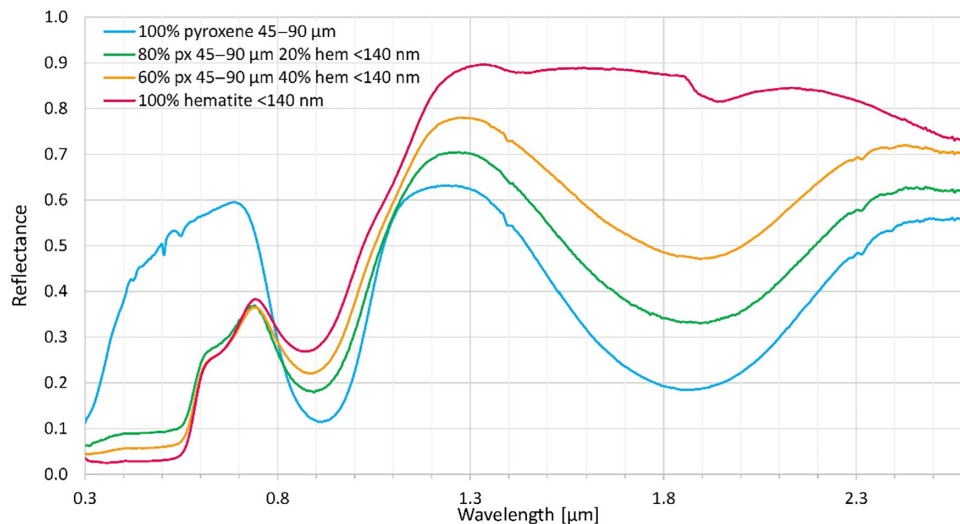
FIGURE 8. Wavelength versus reflectance of hematite, pyroxene, and mixtures thereof. The first major pyroxene absorption experiences a reduction of band strength and a lower overall reflectance in the visible region. (Color figure can be viewed at wileyonlinelibrary.com)

addition, the abundances of hematite and partly pyroxene in these mixtures are much higher than those seen in our study.

Cutler et al. (2020) heated several pyroxenes for various amounts of time under Earth atmospheric conditions. As mentioned before, they likewise observed the formation of hematite for their considered samples, that is, basalt, diopside, augite, pyroxenite, and olivine. They note that hematite took longer to form from pyroxenes than from olivine (about an order of magnitude) and that pyroxene signatures are still recognizable after 2 months of alteration. The authors chose much longer durations for their experiments (1–7 weeks) than shown in this study, yet interestingly likewise observe an increase of reflectance and pyroxene band strength even with respect to the unheated sample. The orthopyroxenite sample showed an increase of 20% in pyroxene band depth and a slight increase in overall reflectance, which the authors attribute to the formation of relatively brighter hematite in their case. The diopside sample even shows larger increases in band depth, which was suggested to form due to two possible mechanisms: (1) The migration of iron from the inner pyroxene grains to form hematite brings more Fe near or to the surface of the grains which results in the appearance of an increased iron abundance, and (2) the cations in the initial pyroxene might be disordered and at elevated temperatures, more Fe can migrate to the preferred M2 sites. Both scenarios would cause an intensification of the pyroxene absorptions. For the diopside sample, Cutler et al. (2020) observe a shift to longer wavelength with increasing durations. They attribute this to the possibly higher iron abundance in the M2 site or the iron

migration toward the grain surfaces. However, the pyroxene absorption of their orthopyroxenite sample appears to narrow and slightly shift to shorter wavelength, which they do not describe but is observable in their Figure 1. In summary, their results strongly suggest that an oxidation process is also driving the spectral change in our experiments.

The most systematic and distinct changes for our laboratory heating experiments were observed when comparing heated surfaces and heated interiors. All meteoritic regolith analogs showed that for a certain threshold temperature/duration, both reflectance and pyroxene band I strength increase for interior versus surface samples. The most likely explanation for the lack of change on the surface is that volatiles lost from Murchison cause the process changing the interior analog sample, yet are quickly lost to the applied near-vacuum on and/or near the surface. In the interior, volatiles are more likely to interact with the surrounding material with no alternative to escape. The mentioned threshold temperatures of the experiments were mostly around 400°C, suggesting that the ejecta deposits on Vesta might have experienced temperatures at or above 400°C. However, as we have seen in our experiments, higher reflectance and pyroxene band I strength can already appear at lower temperatures, depending on the material characteristics like volatile-bearing species, volatile abundance, and possibly also characteristics of the reduced pyroxene-bearing species.

Straub et al. (1991) exposed pyroxenes to oxidation and observed the obscuring of the prominent pyroxene crystal field bands as well as the intensification of the Fe^{2+} to Fe^{3+} IVCT transition, yet they did not heat their

pyroxenes simultaneously. They state that the Fe^{3+} cation can both remain within the pyroxene structure or leave the structure to form nanophase hematite.

McCanta and Dyar (2020) showed that increased oxidation (higher Fe^{3+}) of pyroxenes leads to band minima at shorter wavelengths, although they did not observe the formation of hematite. They likewise did not observe an increase in reflectance and pyroxene band strength with progressive oxidation, in contrast to what Cutler et al. (2020) showed. However, Cutler et al. (2020) applied significant temperatures to the samples while exposing them to an oxidizing environment, which likely plays a key role in the observed increase in reflectance and pyroxene band strength.

Pyroxene band position shifts to shorter or longer wavelengths (indicated by the 0.965/0.917 [µm] ratio) do not follow a systematic trend, neither for the laboratory acquired spectra of heated samples shown in this study nor for PIDs on Vesta (Michalik, Stephan, et al., 2022). We speculate that two processes occur at the same time while counterbalancing each other, leading to the observed subtle shifts and inconsistent observations. Oxidation and the formation of hematite would shift band positions to shorter wavelengths whereas Fe^{2+} enrichment in M2 crystallographic sites would shift band centers to longer wavelengths. The resulting shifts of band positions are possibly caused by each process being dominant for each individual setting. In our experiments, this might be caused by different temperatures, heating durations, mixture compositions or the given proportions of pyroxene-rich endogenic and volatile-bearing exogenic analogs. These attributes can also vary on Vesta for different PID locations. Nevertheless, the observed shifts to shorter or longer wavelengths are very small (typically <0.5%) and thus might be insignificant altogether. We refrained from calculating band positions of the second pyroxene absorption in the presented experiments as the spectra appear quite distorted near the band minima.

Observations in View of PIDs on Vesta

As stated before, the surrounding ejecta deposits are likely of the same age and initial composition as the PIDs themselves while PIDs likely consist of particles released from the inner deposit (Boyce et al., 2012; Denevi et al., 2012; Michalik et al., 2021; Tornabene et al., 2012). Consequently, it can be assumed that the surrounding impact deposits likewise experienced higher temperatures upon deposition, but possibly not reaching the same peak temperature as the interior, and/or the same duration of elevated temperatures and/or the same extent of accumulated material beneath the surface (which is critical for PID formation). This emphasizes the results of

this study regarding the differences between interiors and surfaces of heated samples and comparisons between different durations and/or temperatures. Our results show that the most indicative comparison is that of interiors versus surfaces, whereas differences in temperatures and/or durations do not systematically lead to changes consistent with PIDs on Vesta. Again, the *true* values of interiors are expected to be even more different from the surfaces', as interior particles could only be measured as a mixture of interior and surface particles.

As shown in this study, temperatures needed for the observed spectral changes to occur can vary substantially, depending mostly on the materials' properties and the abundance of volatile-bearing material. Another factor that distinguishes the two settings (laboratory and Vesta), of course, is time and scale. The PIDs associated with Marcia have been exposed to the space environment for at least 40 Ma (Williams, Jaumann, et al., 2014), which the meteoritic samples, after heating, have not. It is possible that large visible slopes degrade over time, which is characteristic for space weathering on Vesta (Pieters et al., 2012). Pieters et al. (2012) have shown that typical soil maturation characteristics (like reddening of spectrum and loss of spectral features) prevailing on the Moon and some asteroids do not prevail on Vesta. Instead, freshly exposed bright areas are relatively redder than background soil, with mechanical brecciation and blending with other constituents dominating the degradation of spectra (decrease of reflectance and diminishment of absorption bands; Pieters et al., 2012).

Moreover, hematite might not have been able to have fully formed in this environment or to have formed in spectrally significant quantities, as previously stated. Our experiments showed that hematite can already form at temperatures as low as 200°C, yet our analog samples are homogeneously mixed particulate materials, whereas the impact deposits on Vesta probably contain both melt and rock fragments, inhomogeneously mixed with CC-material. Jaumann et al. (2014) have shown that the "dark material" on Vesta often occurs as heterogeneously distributed lenses in the subsurface/regolith, which probably changes the material's behavior. Furthermore, we have no way of knowing the *real* composition of the CC-material within the regolith around Marcia. Different (carbonaceous) chondrite types could alter the oxidation behavior, which the presented laboratory experiments have likewise shown. As discussed before, the oxidation process appears highly sensitive to the species of CC material and its abundance. Moreover, hematite is just one of many iron (hydr-)oxides that can form upon oxidation; thus, a different product could have formed on Vesta that does not feature such a strong increase in visible slope. In this regard, we note that oxygen fugacity cannot be monitored or modified in the used facility.

Oxygen fugacity might influence the reactive behavior of the used samples and thus can have effects on the phases that occur as products. Future experiments in a facility capable of modifying oxygen fugacities could confirm our results for Vesta or shed light on other possible reaction outcomes.

Lastly, our experiments show that even the 2 h heating experiments show significant alteration when the temperature is high enough. However, little is known about the temperatures and cooling times that the Marcia ejecta experienced. Detailed modeling of the Marcia impact and its ejecta deposition would improve our understanding of the initial heating and subsequent cooling histories as well as possible impactor material (volatile-bearing) survival.

In spite of these potentially complicating factors, systematic spectral variations are seen and can be assigned to plausible mechanisms. This study suggests that some factors related to heating dominate the spectral changes, particularly the formation of iron oxyhydroxides, facilitated by the presence of volatile-bearing carbonaceous chondrites, and migration of Fe^{2+} within mineral phases.

SUMMARY AND CONCLUSIONS

Pitted impact deposits (PIDs) on Vesta show higher reflectances and pyroxene band strengths with respect to their surroundings. Many of the heating experiments shown in this work are able to reproduce these spectral signatures. The most systematic and pronounced changes regarding these spectral characteristics occur when comparing the interiors of heated meteoritic regolith analogs with their surfaces, that is, the interiors exhibit higher reflectances and higher pyroxene band strengths. This appears intuitive as the PIDs' surfaces likely represent material from the interior of their impact deposit.

In addition to higher reflectance and band strength, we observe the formation of hematite accompanied by an increase of the visible slope. The formation of hematite indicates an oxidation process occurring within the sample due to the presence of volatiles, likely causing the observed spectral changes. In addition to the formation of hematite, the oxidation in combination with heat could enable the migration of iron cations within their host pyroxene grains either to the preferred M2 crystallographic sites or to the grain edges, thus intensifying the pyroxene absorptions. This simple subsolidus thermal oxidation process is the most likely explanation for the distinct spectral characteristics of PIDs which deviate from typical Vestan values, especially as other more plausible options like differences in age, grain size, or roughness have already been ruled out.

However, the exact intra-crystal mechanism causing the increase of the pyroxene band I strength remains under debate and will be subject to future analytical work.

Hematite was recently suggested to also be present on Psyche (Kleer et al., 2021) and was recently detected on the Moon (Li et al., 2020). Hence, oxidation processes might be more widespread in the solar system than previously thought. We suggest that Vesta may not be the only object where the interiors of impact deposits look different than their surfaces, apart from space weathering processes. Thus, we might be forced to carefully reconsider our conclusions about impact deposits from remote spectral observations.

Conflict of Interest Statement—The authors declare no conflict of interest.

Data Availability Statement—The spectra of the various samples/temperatures/durations presented in this study are available from the corresponding author upon request.

Editorial Handling—Dr. Carle M. Pieters

REFERENCES

Adams, J. B., and Filice, A. L. 1967. Spectral Reflectance 0.4 to 2.0 Microns of Silicate Rock Powders. *Journal of Geophysical Research* 72: 5705–15. https://doi.org/10.1029/JZ072i022p05705.

Alemanno, G., Maturilli, A., Helbert, J., and D'Amore, M. 2020. Laboratory Studies on the 3 μm Spectral Features of

Mg-Rich Phyllosilicates with Temperature Variations in Support of the Interpretation of Small Asteroid Surface Spectra. *Earth and Planetary Science Letters* 546: 116424. https://doi.org/10.1016/j.epsl.2020.116424.

Bland, P. A., Cressey, G., and Menzies, O. N. 2004. Modal Mineralogy of Carbonaceous Chondrites by X-Ray Diffraction and Mössbauer Spectroscopy. *Meteoritics & Planetary Science* 39: 3–16. https://doi.org/10.1111/j.1945-5100.2004.tb00046.x.

Boyce, J. M., Wilson, L., Mouginis-Mark, P. J., Hamilton, C. W., and Tornabene, L. L. 2012. Origin of Small Pits in Martian Impact Craters. *Icarus* 221: 262–275. https://ui.adsabs.harvard.edu/abs/2012Icar..221..262B.

Burbine, T. H., Buchanan, P. C., Binzel, R. P., Bus, S. J., Hiroi, T., Hinrichs, J. L., Meibom, A., and Mccoy, T. J. 2001. Vesta, Vestoids, and the Howardite, Eucrite, Diogenite Group: Relationships and the Origin of Spectral Differences. *Meteoritics & Planetary Science* 36: 761–781. https://doi.org/10.1111/j.1945-5100.2001.tb01915.x.

Burns, R. G. 1993. *Mineralogical Applications of Crystal Field Theory*. New York: Cambridge University Press.

Clark, R. N. 1999. Spectroscopy of Rocks and Minerals, and Principles of Spectroscopy. In *Remote Sensing for the Earth Sciences: Manual of Remote Sensing*, edited by A. N. Rencz, vol. 3. John Wiley & Sons, Inc., New York.

Cloutis, E. A., Hudon, P., Hiroi, T., and Gaffey, M. J. 2012. Spectral Reflectance Properties of Carbonaceous Chondrites 4: Aqueously Altered and Thermally Metamorphosed Meteorites. *Icarus* 220: 586–617. https://doi.org/10.1016/j.icarus.2012.05.018.

Cloutis, E. A., Izawa, M. R. M., Pompilio, L., Reddy, V., Hiesinger, H., Nathues, A., Mann, P., le Corre, L., Palomba, E., and Bell, J. F., III. 2013. Spectral Reflectance Properties of HED Meteorites + CM2 Carbonaceous Chondrites: Comparison to HED Grain Size and Compositional Variations and Implications for the Nature of Low-Albedo Features on Asteroid 4 Vesta. *Icarus* 223: 850–877. http://adsabs.harvard.edu/abs/2013Icar..223..850C.

Combe, J.-P., Ammannito, E., Tosi, F., De Sanctis, M. C., McCord, T. B., Raymond, C. A., et al. 2015. Reflectance Properties and Hydrated Material Distribution on Vesta: Global Investigation of Variations and their Relationship Using Improved Calibration of Dawn VIR Mapping Spectrometer. *Icarus* 259: 21–38. http://adsabs.harvard.edu/abs/2015Icar..259...21C.

Consolmagno, G. J., and Drake, M. J. 1977. Composition and Evolution of the Eucrite Parent Body: Evidence from Rare Earth Elements. *Geochimica et Cosmochimica Acta* 41: 1271–82. https://doi.org/10.1016/0016-7037(77)90072-2.

Cutler, K. S., Filiberto, J., Treiman, A. H., and Trang, D. 2020. Experimental Investigation of Oxidation of Pyroxene and Basalt: Implications for Spectroscopic Analyses of the Surface of Venus and the Ages of Lava Flows. *The Planetary Science Journal* 1: 21. https://doi.org/10.3847/PSJ/ab8faf.

De Sanctis, M. C., Ammannito, E., Capria, M. T., Tosi, F., Capaccioni, F., Zambon, F., et al. 2012. Spectroscopic Characterization of Mineralogy and its Diversity across Vesta. *Science* 336: 697–700. https://doi.org/10.1126/science.1219270.

De Sanctis, M. C., Combe, J.-P., Ammannito, E., Palomba, E., Longobardo, A., McCord, T. B., et al. 2012. Detection of Widespread Hydrated Materials on Vesta by the VIR Imaging Spectrometer on Board the Dawn Mission. *The Astrophysical Journal Letters* 758: L36. http://adsabs.harvard.edu/abs/2012ApJ...758L..36D.

Denevi, B. W., Blewett, D. T., Buczkowski, D. L., Capaccioni, F., Capria, M. T., De Sanctis, M. C., et al. 2012. Pitted Terrain on Vesta and Implications for the Presence of Volatiles. *Science* 338: 246–49. https://doi.org/10.1126/science.1225374.

Dixit, A., Bhatia, B., and Tripathi, R. P. 2021. Evolution of Hematite and/or Magnetite Iron Phases with Thermal Heating in Ordinary Chondrites: A Generic Characteristic. *Journal of Earth System Science* 130: 191. https://doi.org/10.1007/s12040-021-01699-8.

Fendrich, K. V., and Ebel, D. S. 2021. Comparison of the Murchison CM2 and Allende CV3 Chondrites. *Meteoritics & Planetary Science* 56: 77–95. https://doi.org/10.1111/maps.13623.

Galiano, A., Dirri, F., Palomba, E., Longobardo, A., Schmitt, B., and Beck, P. 2020. Spectral Investigation of Ceres Analogue Mixtures: In-Depth Analysis of Crater Central Peak Material (ccp) on Ceres. *Icarus* 343: 113692. https://ui.adsabs.harvard.edu/abs/2020Icar..34313692G.

Harloff, J., and Arnold, G. 2001. Near-Infrared Reflectance Spectroscopy of Bulk Analog Materials for Planetary Crust. *Planetary and Space Science* 49: 191–211. https://doi.org/10.1016/s0032-0633(00)00132-x.

Helbert, J., and Maturilli, A. 2008. *The Heat is on—In the Planetary Emissivity Laboratory (PEL) at DLR Berlin*. Paper presented at the European Planetary Science Congress 2008. http://adsabs.harvard.edu/abs/2008epsc.conf..934H.

Hinrichs, J. L., and Lucey, P. G. 2002. Temperature-Dependent Near-Infrared Spectral Properties of Minerals, Meteorites, and Lunar Soil. *Icarus* 155: 169–180. https://doi.org/10.1006/icar.2001.6754.

Hiroi, T., Pieters, C. M., Zolensky, M. E., and Lipschutz, M. E. 1993. Evidence of Thermal Metamorphism on the C, G, B, and F Asteroids. *Science* 261: 1016–18. https://doi.org/10.1126/science.261.5124.1016.

Hiroi, T., Pieters, C. M., Zolensky, M. E., and Lipschutz, M. E. 1994. Possible Thermal Metamorphism on the C, G, B, and F Asteroids Detected from their Reflectance Spectra in Comparison with Carbonaceous Chondrites. *Antarctic Meteorite Research* 7: 230.

Hiroi, T., and Zolensky, M. E. 1999. UV-Vis-NIR Absorption Features of Heated Phyllosilicates as Remote-Sensing Clues of Thermal Histories of Primitive Asteroids. *Antarctic Meteorite Research* 12: 108. https://ui.adsabs.harvard.edu/abs/1999AMR....12..108H.

Huguenin, R. L., Adams, J. B., and McCord, T. B. 1977. *Mars: Surface Mineralogy from Reflectance Spectra*. https://ui.adsabs.harvard.edu/abs/1977LPI.....8..478H.

Hunt, G. R. 1977. Spectral Signatures of Particulate Minerals in the Visible and Near Infrared. *Geophysics* 42: 501–513. https://doi.org/10.1190/1.1440721.

Jaumann, R., Nass, A., Otto, K., Krohn, K., Stephan, K., McCord, T. B., Williams, D. A., et al. 2014. The Geological Nature of Dark Material on Vesta and Implications for the Subsurface Structure. *Icarus* 240: 3–19. https://doi.org/10.1016/j.icarus.2014.04.035.

Keil, K. 2002. Geological History of Asteroid 4 Vesta: The "Smallest Terrestrial Planet". In *Asteroids III*: 573–584. Tucson: University of Arizona Press.

Kleer, K. D., Cambioni, S., and Shepard, M. 2021. The Surface of (16) Psyche from Thermal Emission and

Polarization Mapping. *The Planetary Science Journal* 2: 149. https://doi.org/10.3847/PSJ/ac01ec.

Larson, H. P., and Fink, U. 1975. Infrared Spectral Observations of Asteroid 4 Vesta. *Icarus* 26: 420–27. https://doi.org/10.1016/0019-1035(75)90109-8.

Li, S., Lucey, P. G., Fraeman, A. A., Poppe, A. R., Sun, V. Z., Hurley, D. M., and Schultz, P. H. 2020. Widespread Hematite at High Latitudes of the Moon. *Science Advances* 6: eaba1940. https://doi.org/10.1126/sciadv.aba1940.

Maturilli, A., Helbert, J., and Arnold, G. 2019. *The Newly Improved Set-Up at the Planetary Spectroscopy Laboratory (PSL)*. Paper presented at the Infrared Remote Sensing and Instrumentation XXVII.

McCanta, M. C., and Dyar, M. D. 2020. Effects of Oxidation on Pyroxene Visible-Near Infrared and Mid-Infrared Spectra. *Icarus* 352: 113978. https://doi.org/10.1016/j.icarus.2020.113978.

McCord, T. B., Adams, J. B., and Johnson, T. V. 1970. Asteroid Vesta: Spectral Reflectivity and Compositional Implications. *Science* 168: 1445–47. http://adsabs.harvard.edu/abs/1970Sci...168.1445M.

McCord, T. B., Li, J.-Y., Combe, J.-P., McSween, H. Y., Jaumann, R., Reddy, V., Tosi, F., et al. 2012. Dark Material on Vesta from the Infall of Carbonaceous Volatile-Rich Material. *Nature* 491: 83–86. https://doi.org/10.1038/nature11561.

McSween, H. Y. 1979. Alteration in CM Carbonaceous Chondrites Inferred from Modal and Chemical Variations in Matrix. *Geochimica et Cosmochimica Acta* 43: 1761–70. https://doi.org/10.1016/0016-7037(79)90024-3.

Michalik, T., Maturilli, A., Cloutis, E. A., Matz, K.-D., Milke, R., Stephan, K., et al. 2022. *Laboratory Heating of HED + CC Mixtures Indicates Localized Oxidation on Vesta*. Paper Presented at the Lunar and Planetary Science Conference, Houston, TX, USA. https://www.hou.usra.edu/meetings/lpsc2022/pdf/2248.pdf.

Michalik, T., Matz, K.-D., Schröder, S. E., Jaumann, R., Stephan, K., Krohn, K., Preusker, F., Raymond, C. A., Russell, C. T., and Otto, K. A. 2021. The Unique Spectral and Geomorphological Characteristics of Pitted Impact Deposits Associated with Marcia Crater on Vesta. *Icarus* 369: 114633. https://doi.org/10.1016/j.icarus.2021.114633.

Michalik, T., Stephan, K., Cloutis, E. A., Matz, K.-D., Jaumann, R., Raponi, A., and Otto, K. A. 2022. The Spectral Properties of Pitted Impact Deposits on Vesta as Seen by the Dawn VIR Instrument. *The Planetary Science Journal* 3: 182. https://doi.org/10.3847/PSJ/ac7be0.

Minitti, M. E., Mustard, J. F., and Rutherford, M. J. 2002. Effects of Glass Content and Oxidation on the Spectra of SNC-Like Basalts: Applications to Mars Remote Sensing. *Journal of Geophysical Research: Planets* 107(E5): 6. https://doi.org/10.1029/2001JE001518.

Mittlefehldt, D. W. 2015. Asteroid (4) Vesta: I. The Howardite-Eucrite-Diogenite (HED) Clan of Meteorites. *Chemie der Erde-Geochemistry* 75: 155–183. https://doi.org/10.1016/j.chemer.2014.08.002.

Miyamoto, H., Niihara, T., Wada, K., Ogawa, K., Senshu, H., Michel, P., et al. 2021. Surface Environment of Phobos and Phobos Simulant UTPS. *Earth, Planets and Space* 73(1): 214. https://doi.org/10.1186/s40623-021-01406-3.

Miyamoto, M., and Mikouchi, T. 2001. Diffuse Reflectance Spectra of a Eucrite: Resistance to Heating at Different Oxygen Fugacities, Lunar and Planetary Science Conference, XXXII, Abstract #1261, Lunar Planet. Inst., Houston, Texax.

Morris, R. V., Agresti, D. G., Lauer, H. V., Jr., Newcomb, J. A., Shelfer, T. D., and Murali, A. V. 1989. Evidence for Pigmentary Hematite on Mars Based on Optical, Magnetic, and Mossbauer Studies of Superparamagnetic (Nanocrystalline) Hematite. *Journal of Geophysical Research: Solid Earth* 94(B3): 2760–78. https://doi.org/10.1029/JB094iB03p02760.

Morris, R. V., Bell, J. F., III, and Lauer, H. V., Jr. 1994. Hematite Formed from Pyroxene on Mars by Meteoritic Impact, Abstracts of the 25th Lunar and Planetary Science Conference, p. 939, Houston, Texas.

Morris, R. V., Golden, D. C., Bell, J. F., III, Shelfer, T. D., Scheinost, A. C., Hinman, N. W., Furniss, G., et al. 2000. Mineralogy, Composition, and Alteration of Mars Pathfinder Rocks and Soils: Evidence from Multispectral, Elemental, and Magnetic Data on Terrestrial Analogue, SNC Meteorite, and Pathfinder Samples. *Journal of Geophysical Research: Planets* 105(E1): 1757–1817. https://doi.org/10.1029/1999JE001059.

Morris, R. V., Lauer, H. V., Jr., Lawson, C. A., Gibson, E. K., Jr., Nace, G. A., and Stewart, C. 1985. Spectral and Other Physicochemical Properties of Submicron Powders of Hematite (α-Fe_2O_3), Maghemite (γ-Fe_2O_3), Magnetite (Fe_3O_4), Goethite (α-FeOOH), and Lepidocrocite (γ-FeOOH). *Journal of Geophysical Research: Solid Earth* 90(B4): 3126–44. https://doi.org/10.1029/JB090iB04p03126.

Palomba, E., Longobardo, A., De Sanctis, M. C., Zambon, F., Tosi, F., Ammannito, E., et al. 2014. Composition and Mineralogy of Dark Material Units on Vesta. *Icarus* 240: 58–72. https://doi.org/10.1016/j.icarus.2014.04.040.

Pieters, C. M., Ammannito, E., Blewett, D. T., Denevi, B. W., de Sanctis, M. C., Gaffey, M. J., le Corre, L., et al. 2012. Distinctive Space Weathering on Vesta from Regolith Mixing Processes. *Nature* 491: 79–82. https://doi.org/10.1038/nature11534.

Poch, O., Pommerol, A., Jost, B., Carrasco, N., Szopa, C., and Thomas, N. 2016. Sublimation of Water Ice Mixed with Silicates and Tholins: Evolution of Surface Texture and Reflectance Spectra, with Implications for Comets. *Icarus* 267: 154–173. https://ui.adsabs.harvard.edu/abs/2016Icar..267..154P.

Reddy, V., Le Corre, L., O'Brien, D. P., Nathues, A., Cloutis, E. A., Durda, D. D., et al. 2012. Delivery of Dark Material to Vesta Via Carbonaceous Chondritic Impacts. *Icarus* 221: 544–559. https://doi.org/10.1016/j.icarus.2012.08.011.

Roatsch, T., Kersten, E., Matz, K.-D., Preusker, F., Scholten, F., Elgner, S., Jaumann, R., Raymond, C. A., and Russell, C. T. 2013. High-Resolution Vesta Low Altitude Mapping Orbit Atlas Derived from Dawn Framing Camera Images. *Planetary and Space Science* 85: 293–98. http://adsabs.harvard.edu/abs/2013P%26SS...85..293R.

Ruesch, O., Hiesinger, H., Cloutis, E., Le Corre, L., Kallisch, J., Mann, P., et al. 2015. Near Infrared Spectroscopy of HED Meteorites: Effects of Viewing Geometry and Compositional Variations. *Icarus* 258: 384–401. https://doi.org/10.1016/j.icarus.2015.06.034.

Ruzicka, A., Snyder, G. A., and Taylor, L. A. 1997. Vesta as the HED Parent Body: Implications for the Size of a Core and for Large-Scale Differentiation. *Meteoritics &*

Planetary Science 32: 825–840. http://adsabs.harvard. edu/abs/1997M%26PS...32..825R.

Sidhu, S., Cloutis, E. A., Mann, P., Applin, D., Hiroi, T., Mengel, K., Kareta, T., Reddy, V., Beck, P., and Mertzman, S. A. 2023. Spectral and Mineralogical Effects of Heating on CM Chondrite and Related Asteroids. *Icarus* 398: 115522. https://doi.org/10.1016/j.icarus.2023. 115522.

Sierks, H., Keller, H. U., Jaumann, R., Michalik, H., Behnke, T., Bubenhagen, F., Büttner, I., et al. 2011. The Dawn Framing Camera. *Space Science Reviews* 163: 263–327. https://doi.org/10.1007/s11214-011-9745-4.

Sizemore, H. G., Platz, T., Schorghofer, N., Prettyman, T. H., De Sanctis, M. C., Crown, D. A., et al. 2017. Pitted Terrains on (1) Ceres and Implications for Shallow Subsurface Volatile Distribution. *Geophysical Research Letters* 44: 6570–78. https://ui.adsabs.harvard. edu/abs/2017GeoRL..44.6570S.

Straub, D. A. W., Burns, R. G., and Pratt, S. F. 1991. Spectral Signature of Oxidized Pyroxenes: Implications to Remote Sensing of Terrestrial Planets. *Journal of Geophysical Research: Planets* 96(E3): 18819–30. https://doi.org/10.1029/91JE01893.

Tompkins, S., and Pieters, C. M. 2010. Spectral Characteristics of Lunar Impact Melts and Inferred Mineralogy. *Meteoritics & Planetary Science* 45: 1152–69. https://doi.org/10.1111/j.1945-5100.2010.01074.x.

Tornabene, L. L., Osinski, G. R., McEwen, A. S., Boyce, J. M., Bray, V. J., Caudill, C. M., Grant, J. A., Hamilton, C. W., Mattson, S., and Mouginis-Mark, P. J. 2012. Widespread Crater-Related Pitted Materials on Mars: Further Evidence for the Role of Target Volatiles During the Impact Process. *Icarus* 220: 348–368. https://ui.adsabs. harvard.edu/abs/2012Icar..220..348T.

Williams, D. A., Jaumann, R., McSween, H. Y., Marchi, S., Schmedemann, N., Raymond, C. A., et al. 2014. The Chronostratigraphy of Protoplanet Vesta. *Icarus* 244: 158–165. https://doi.org/10.1016/j.icarus.2014.06.027.

Williams, D. A., O'Brien, D. P., Schenk, P. M., Denevi, B. W., Carsenty, U., Marchi, S., Scully, J. E. C., et al. 2014. Lobate and Flow-Like Features on Asteroid Vesta. *Planetary and Space Science* 103: 24–35. https://doi.org/10. 1016/j.pss.2013.06.017.

Yamashita, S., Nakamura, T., Jogo, K., Matsuoka, M., and Okumura, S. 2015. Progressive Changes in Mineralogy, Reflectance Spectra and Water Contents of Experimentally Heated Murchison at 400, 600, and 900°C, presented at the 78th Annual Meeting of the Meteoritical Society, Berkeley, California, LPI Contribution No. 1856.

Zhang, X. L., Wu, G. J., Zhang, C. L., Xu, T. L., and Zhou, Q. Q. 2015. What is the Real Role of Iron Oxides in the Optical Properties of Dust Aerosols? *Atmospheric Chemistry and Physics* 15: 12159–77. https://doi.org/10. 5194/acp-15-12159-2015.

Zolensky, M. E., Lipschutz, M. E., and Hiroi, T. 1994. Minerology of Artificially Heated Carbonaceous Chondrites, Abstracts of the 25th Lunar and Planetary Science Conference, p. 1567, Houston, Texas.

Zolensky, M. E., Weisberg, M. K., Buchanan, P. C., and Mittlefehldt, D. W. 1996. Mineralogy of Carbonaceous Chondrite Clasts in HED Achondrites and the Moon. *Meteoritics & Planetary Science* 31: 518–537. http://adsabs. harvard.edu/abs/1996M%26PS...31..518Z.

APPENDIX : DETAILED DESCRIPTION OF VNIR REFLECTANCE OBSERVATIONS

In the following, we display all sample spectra, first showing differences between different temperatures and durations (for sample interiors), followed by the differences between heated surfaces and heated interiors of the samples. Endmember spectra are displayed in the latter. Additionally, we display available spectra of the second major pyroxene absorption near 1.9 µm.

A1.1. Temperature Change

Here, we display reflectance spectra of unheated and heated samples and compare the effects of the different applied temperatures, not accounting for surface or interior differences. The heated spectra displayed here are the spectra of the interior samples as they best represent the processes our samples undergo during heating. Figure A1.1 displays spectra of NWA 5748M and NWA 5230M, heated to 2 h, 72 h, and partly 168 h.

For NWA 5748M, the overall reflectance levels are higher for the 2 h experiments and less systematic (decrease of reflectance from 200 to 400°C and a steep increase for 600°C) than those of the 72 h experiments. However, band I strength values (0.750/0.917 [µm]) steadily increase from 200 to 600°C (Table 4) for the 2 h experiments. For the 72 h experiments, reflectance levels are generally lower and the heating sequence behaves more linear in the way that reflectances increase at 0.750 µm. However, band I strengths steadily decrease in this sequence. The normalized spectra (Figure A1.1e) show that the visible slope steadily increases with temperature and time (except for 600°C and 72 h) and that band I strengths are stronger for the 2 h experiments than for the 72 h experiments (for 200°C, there appears to be no significant difference). Thus, a longer duration of heating appears to lead to reduced band I strengths. Band positions tend to slightly shift to shorter wavelengths (indicated by higher 0.965/0.917 [µm] values). As the only difference between the 2 and 72 h experiments is duration of heating, we speculate that the 72 h experiments allowed any reactions to get closer to completion.

Heating of NWA 5230M leads to similar results. Especially for the 600°C experiments, the visible slope changed significantly to higher values. The aliquot that was heated to 400°C for 168 h (1 week) likewise resulted in a very steep visible slope like those heated to 600°C. Higher temperatures yield the highest reflectances at 0.750 µm while the pyroxene band I strength does not increase. Interestingly, the 300°C, 2 and 72 h experiment of NWA5230M yields higher reflectance and pyroxene band I strength than the 400°C, 2 and 72 h of the same meteoritic mixture.
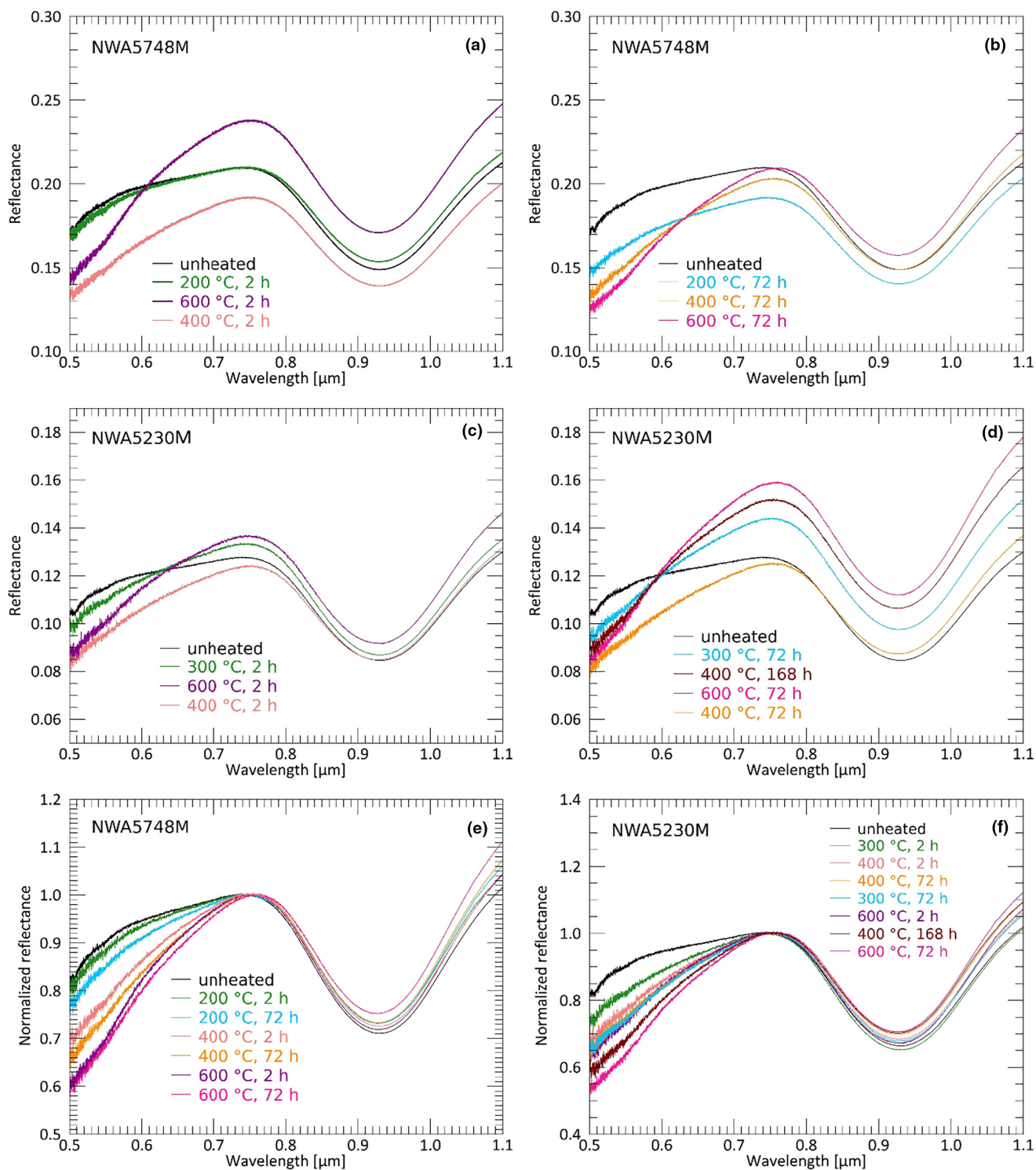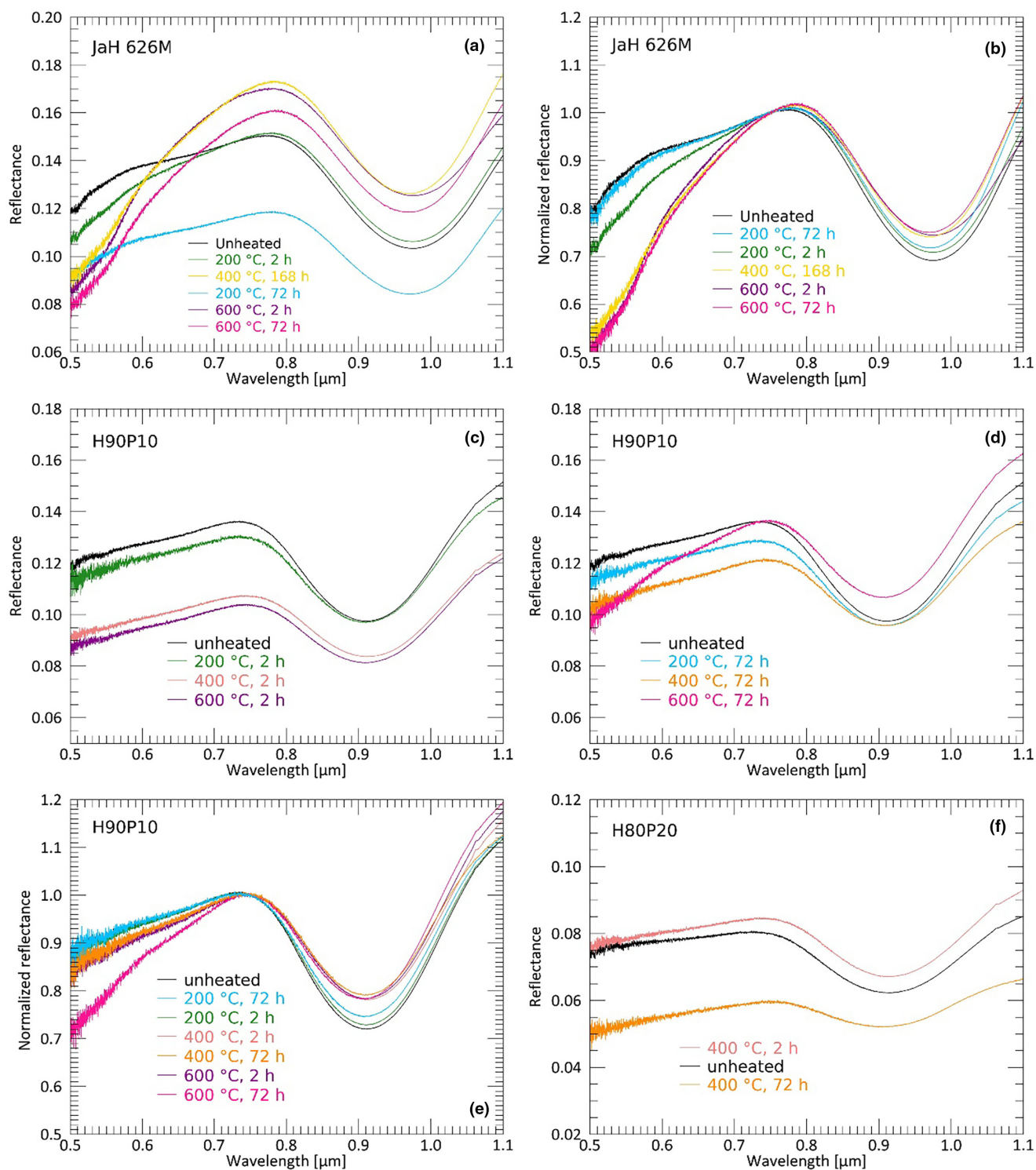
FIGURE A1.1. Wavelength versus reflectance of samples NWA 5748M and NWA 5230M. (a) Absolute reflectance of NWA 5748M, unheated, and after heating to different temperatures for 2 h; (b) absolute reflectance of NWA 5748M, unheated, and after heating to different temperatures for 72 h; (c) absolute reflectance of NWA 5230M, unheated, and after heating to different temperatures for 2 h; (d) absolute reflectance of NWA 5230M, unheated, and after heating to different temperatures for 72 h; (e) normalized spectra at 0.750 µm of NWA 5748M (a and b spectra); (f) normalized spectra at 0.750 µm of NWA 5230M (c and d spectra). (Color figure can be viewed at wileyonlinelibrary.com)

FIGURE A1.2. Wavelength versus reflectance of samples JaH 626M, H90P10, and H80P20. (a) Absolute reflectance of JaH 626M, unheated, and after heating to different temperatures and durations; (b) normalized spectra at 0.750 μm of JaH 626M; (c) absolute reflectance of H90P10, unheated, and after heating to different temperatures for 2 h; (d) absolute reflectance of H90P10, unheated, and after heating to different temperatures for 72 h; (e) normalized spectra at 0.750 μm of H90P10 (c and d spectra); (f) absolute reflectance of H80P20, unheated, and after heating to 400°C for 2 and 72 h. (Color figure can be viewed at wileyonlinelibrary.com)
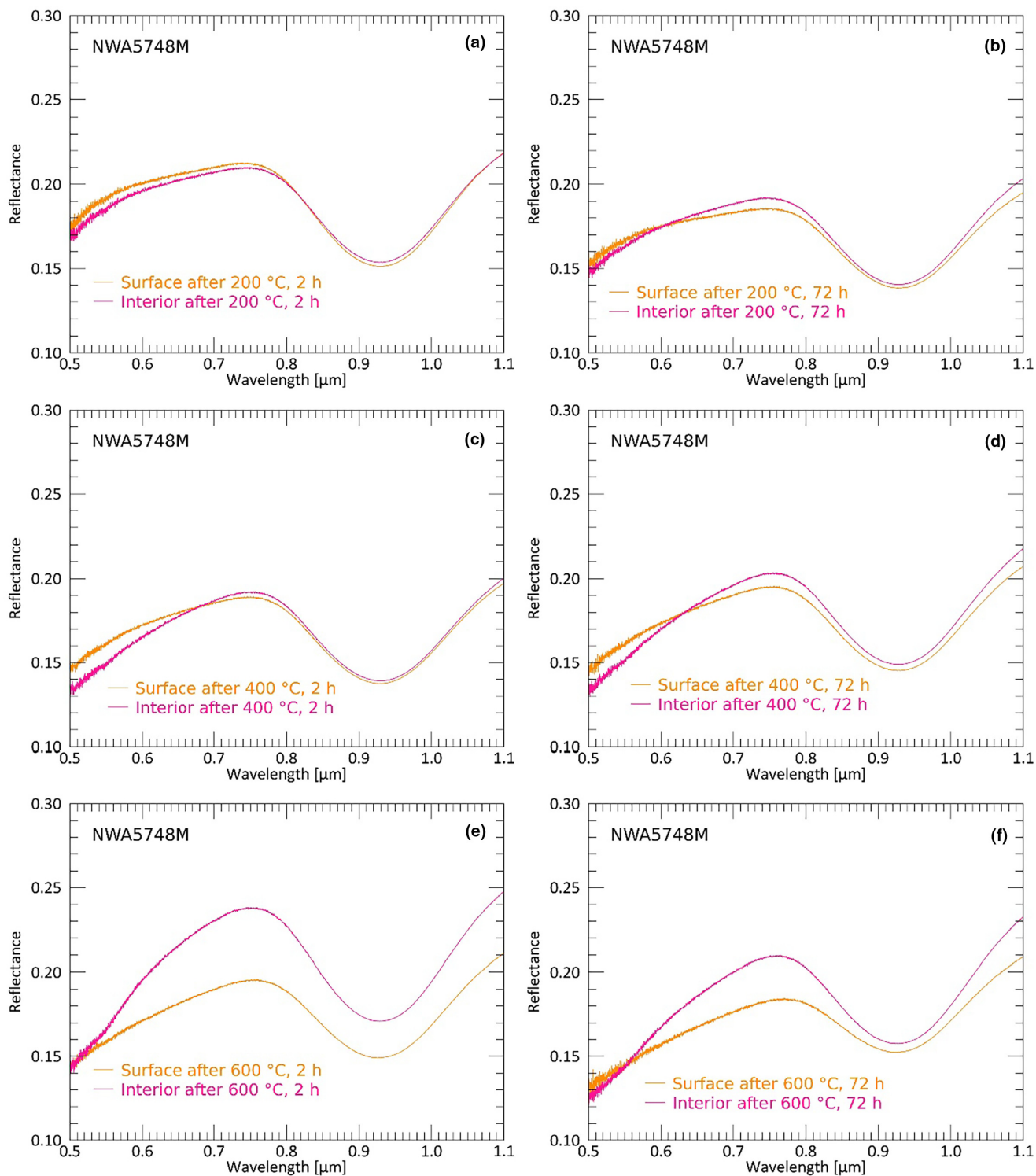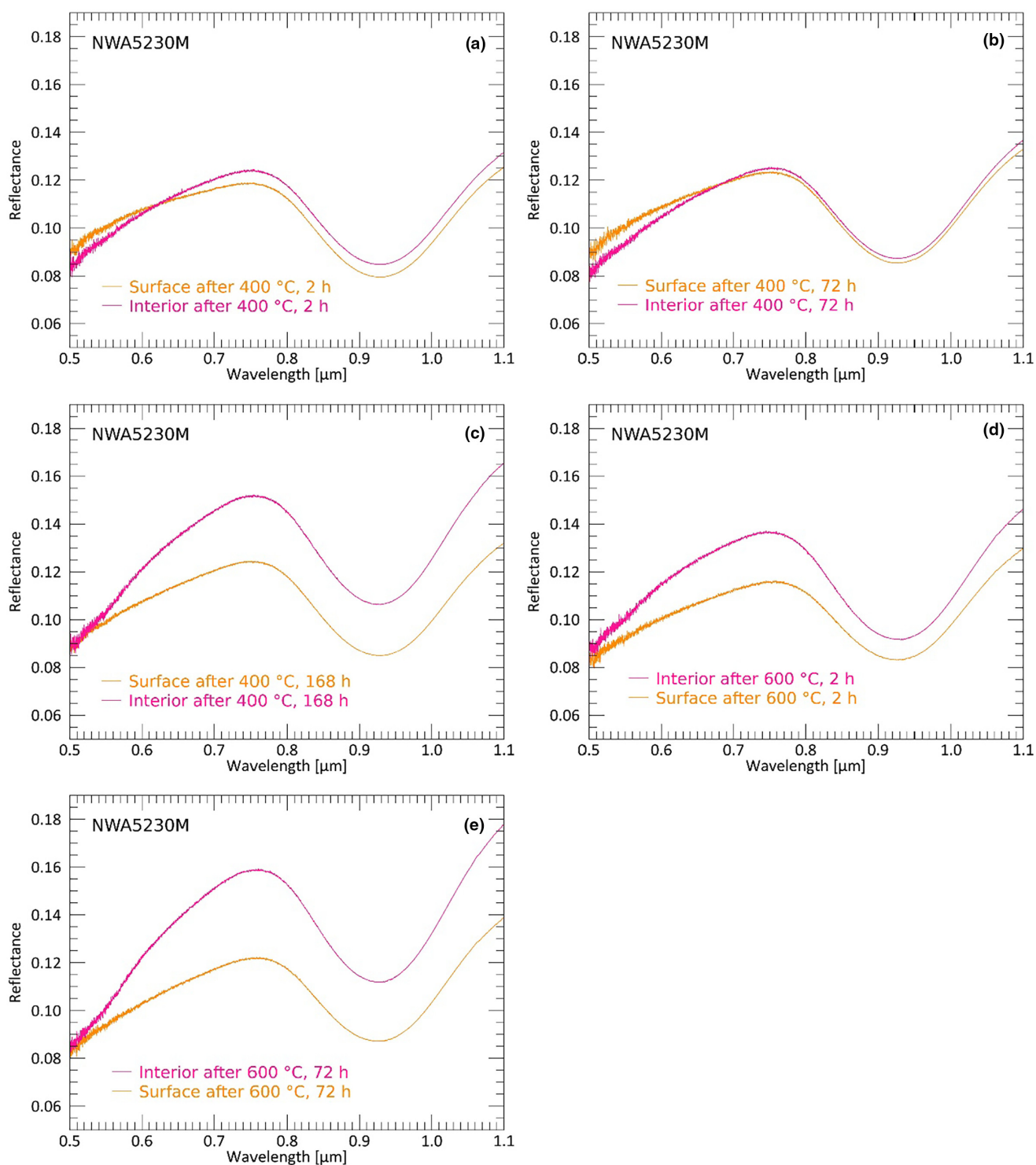
FIGURE A1.3. Wavelength versus reflectance of heated NWA 5748M aliquots. Surface spectra are depicted in orange, interior spectra in pink. (a) 200°C, 2 h, (b) 200°C, 72 h, (c) 400°C, 2 h, (d) 400°C, 72 h, (e) 600°C, 2 h, (f) 600°C, 72 h. (Color figure can be viewed at wileyonlinelibrary.com)

In comparison with the unheated sample, NWA 5230M, 300°C, 2h, is the only heated aliquot to show both higher reflectance at 0.750 μm and pyroxene band I strength (0.750/0.917 [μm]), like the PIDs on Vesta do with respect to their surroundings. However, the surroundings of the PIDs are also impact deposits
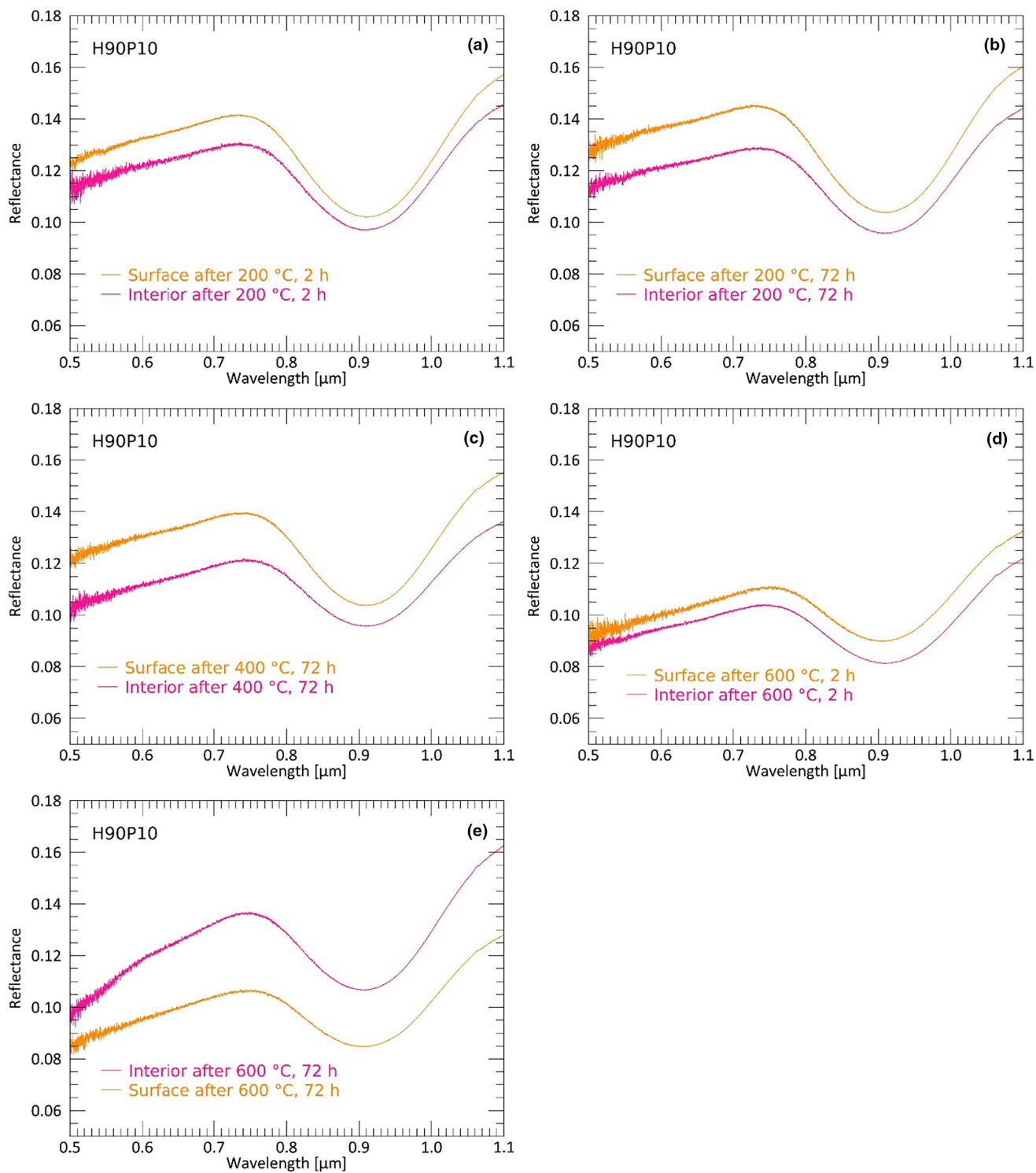
FIGURE A1.4. Wavelength versus reflectance of heated NWA 5230M aliquots. Surface spectra are depicted in orange, interior spectra in pink. (a) 400°C, 2 h, (b) 400°C, 72 h, (c) 400°C, 168 h, (d) 600°C, 2 h, (e) 600°C, 72 h. (Color figure can be viewed at wileyonlinelibrary.com)

(Michalik et al., 2021), likely of the same age and initial composition. Thus, it is worth comparing the heated samples among each other, as well. PIDs likely reveal material from the interior of such impact deposits that was either heated to longer durations or to higher temperatures. Hence, we specifically search for

FIGURE A1.5. Wavelength versus reflectance of heated H90P10 aliquots. Surface spectra are depicted in orange, interior spectra in pink. (a) 200°C, 2 h, (b) 200°C, 72 h, (c) 400°C, 72 h, (d) 600°C, 2 h, (e) 600°C, 72 h. (Color figure can be viewed at wileyonlinelibrary.com)

systematics regarding higher reflectances at 0.750 µm combined with higher pyroxene band I strength for samples that were heated to higher temperatures and/or longer durations with respect to others. However, none of the heated aliquots show these systematics. Especially band I strengths tend to decrease with increasing
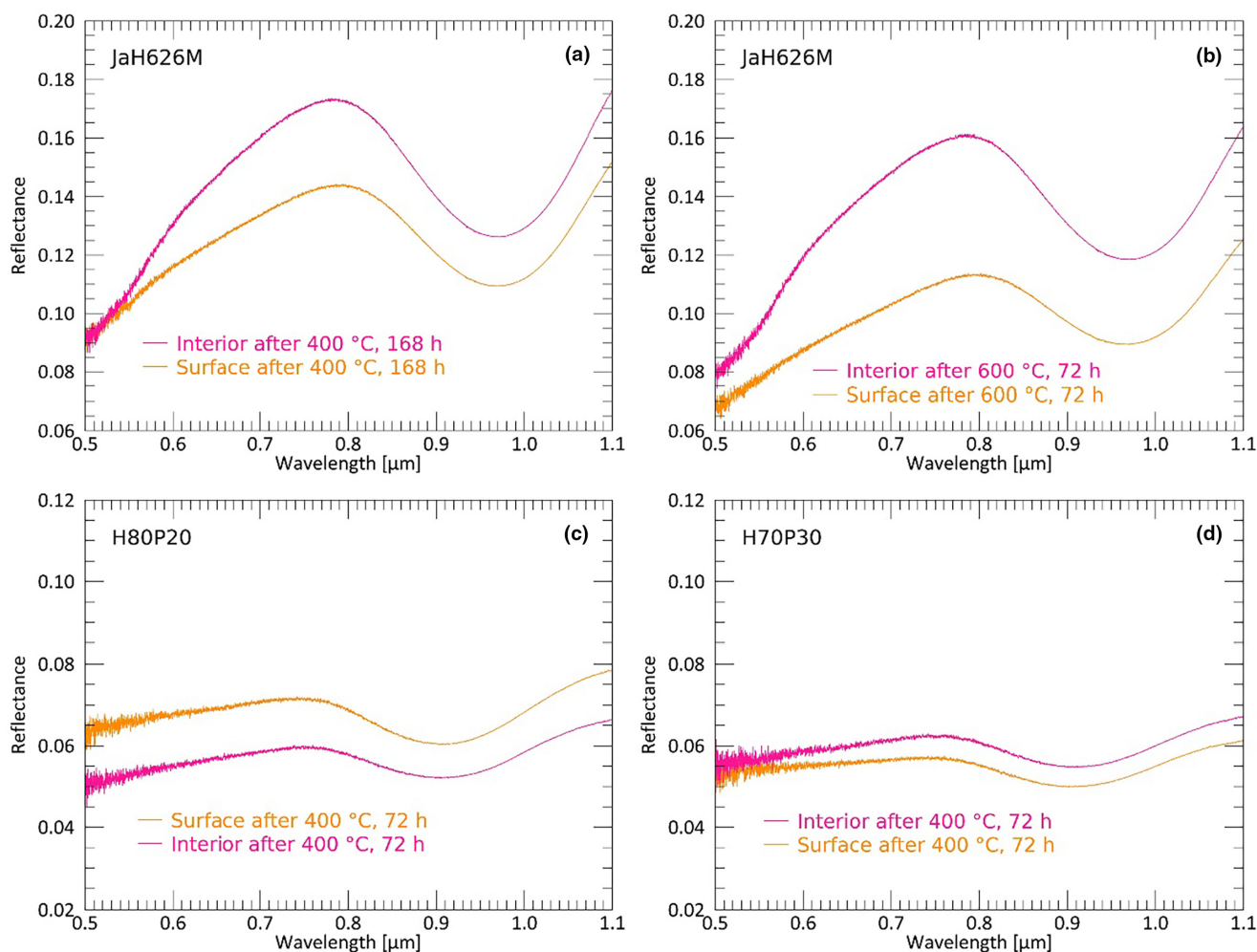
FIGURE A1.6. Wavelength versus reflectance of surface (orange) and interior (pink) samples. (a) JaH 626M, 400°C, 168 h, (b) JaH 626M, 600°C, 72 h, (c) H80P20, 400°C, 72 h, (d) H70P30, 400°C, 72 h. (Color figure can be viewed at wileyonlinelibrary.com)

temperature and duration while reflectance values increase, not matching the situation on Vesta.

Figure A1.2 shows spectra of JaH 626M and the terrestrial analogs H90P10 and H80P20. For H70P30, relevant spectra are shown later in Figures A1.6 and A1.9. This sample was only heated to 400°C for 72 h and the resulting spectrum exhibits lower overall reflectance and lower pyroxene band I strength than the unheated sample. The resampled values are again reported in Table 4.

Similar to the other meteorite mixtures, heated aliquots of JaH 626M show increased visible slopes with increasing temperatures and decreased pyroxene band I strengths with respect to the unheated aliquot. For the terrestrial sample H90P10, only one heated aliquot, 600°C, 72h, shows a significant increase of visible slope and all aliquots show decreased pyroxene band I

strengths with respect to the unheated aliquot (Table 3). Considering heated aliquots among each other, none of the aliquots of JaH 626M or H80P20 show both higher reflectance and pyroxene band I strength with respect to another heated aliquot. For H90P10, the 600°C, 72 h aliquot shows higher reflectance and band I strength with respect to the 400°C, 72 h aliquot.

Differences between Surface and Interior Sample

During the course of the heating experiments, we realized that the surface of heated aliquots had different spectral characteristics than their interiors, which was partly visible to the naked eye as the interiors looked red in contrast to its gray/black surface. We subsequently measured both the reflectance of the surface and interior aliquots, of which the results are shown in the following
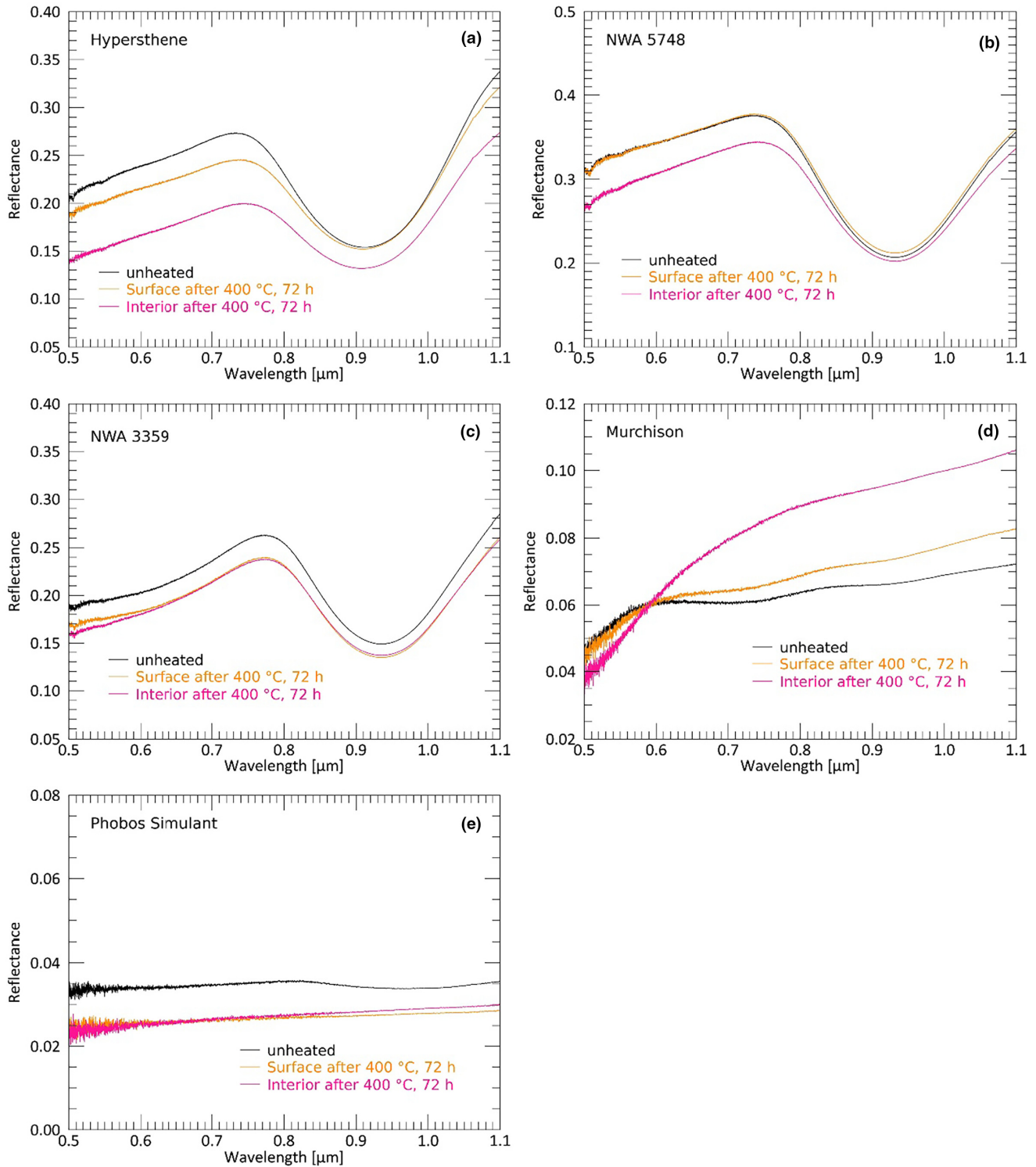
FIGURE A1.7. Wavelength versus reflectance of unheated (black), heated surface (orange), and heated interior (pink) samples of endmember materials. (Color figure can be viewed at wileyonlinelibrary.com)

figures. We start by displaying the same meteoritic and terrestrial samples as in the previous section, followed by spectra representing the endmember meteorites/materials.

Figure A1.3 shows interior and surface spectra of NWA 5748M, heated to different temperatures. With increasing temperature (and partly duration), three
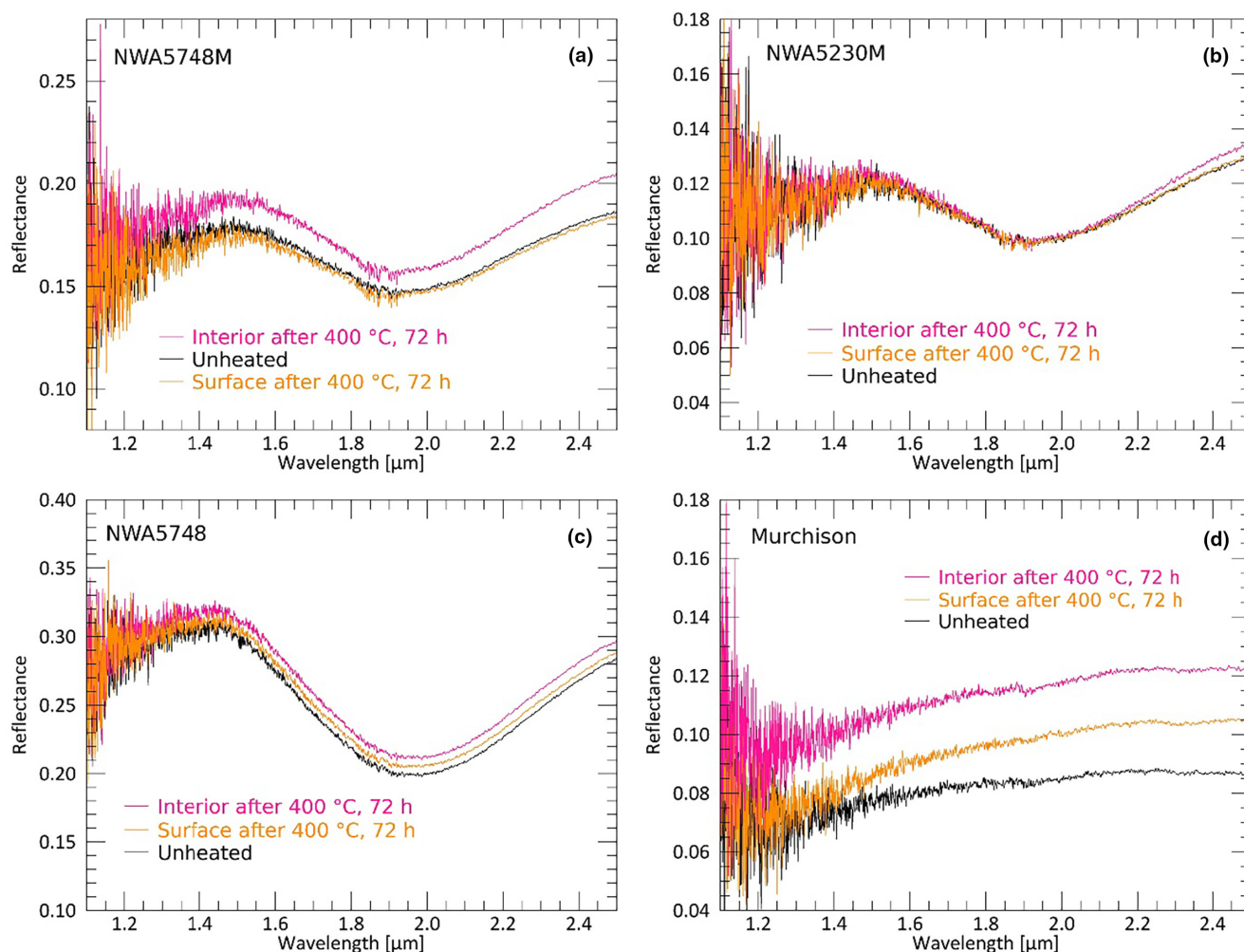
FIGURE A1.8. Wavelength versus reflectance for meteoritic samples displaying the second major pyroxene absorption near 1.9 µm. (a) NWA 5748M, (b) NWA 5230M, (c) NWA 5748, (d) Murchison. All samples show spectra of the unheated as well as heated surface and interior after heating to 400°C and 72 h. (Color figure can be viewed at wileyonlinelibrary.com)

obvious characteristics change: visible slope, reflectance at 0.750 µm, and the pyroxene band I strength all increase for the interior versus the surface. In general, a higher temperature leads to increased visible slopes for both surfaces and interiors. Band positions (0.965/0.917 [µm]) tend to shift to shorter wavelengths for 72 h experiments and to longer wavelengths or hardly any shift for 2 h experiments for interior versus surface spectra.

Figure A1.4 displays spectra of NWA 5230M. Here, reflectance at 0.750 µm, pyroxene band I strength and visible slopes all increase for the 600°C experiments for interior versus surface spectra. Results for the terrestrial mixture H90P10 are shown in Figure A1.5 and for JaH 626M, H80P20, and H70P30 in Figure A1.6. While NWA 5230M shows lower pyroxene band I strength for interior versus surface

spectra after 400°C, 168 h, JaH 626M shows higher pyroxene band I strength after the same time and duration (Table 4). The terrestrial samples do not show a similar significant increase in reflectance, pyroxene band I strength and visible slope for interiors versus surfaces. However, we note that H90P10 shows slightly increased reflectance, pyroxene band I strength, and visible slopes after 600°C, 72 h, and H70P30 shows increased reflectance, pyroxene band I strength, and visible slope already after 400°C, 72 h. Band positions of NWA 5230M, JaH 626M, H90P10, H80P20, and H70P30 all tend to shift to longer wavelengths for interior versus surface. Two experiments (NWA 5230M, 400°C, 168 h and H90P10, 600°C, 72 h) show band positions at slightly shorter wavelengths for the interior versus the surface.
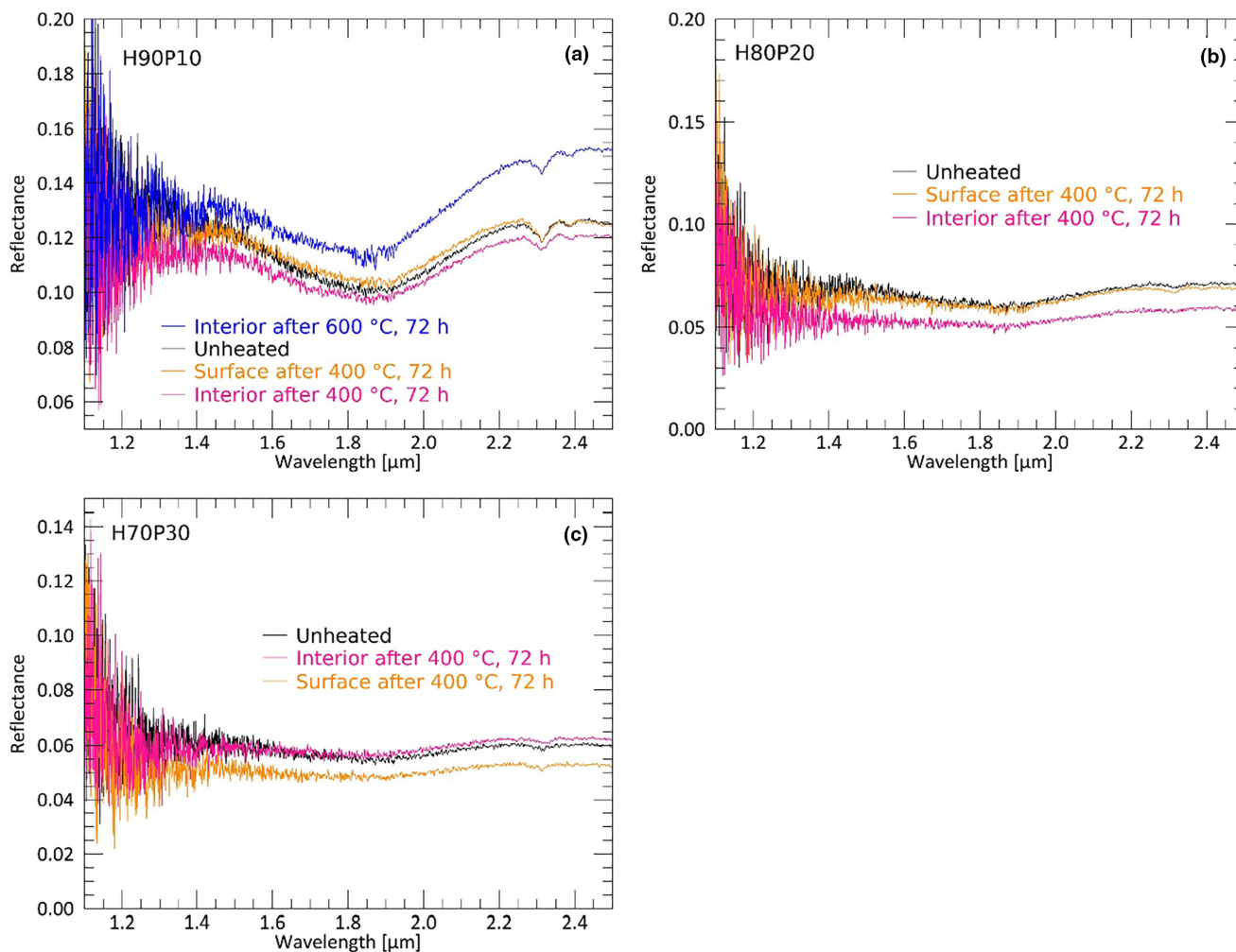
FIGURE A1.9. Wavelength versus reflectance for terrestrial samples displaying the second major pyroxene absorption near 1.9 μm. (a) H90P10, (b) H80P20, (c) H70P30. All samples show spectra of the unheated as well as heated surface and interior after heating to 400°C and 72 h. (a) also shows the spectrum of the interior after heating to 600°C and 72 h. (Color figure can be viewed at wileyonlinelibrary.com)

In the following, spectra of endmember materials are displayed. Figure A1.7 shows spectra of the unheated as well as heated surface and heated interior endmember materials Hypersthene, NWA 5748, NWA 3359, Murchison, and Phobos Simulant. NWA 3359 is considered an endmember as it had not been mixed with any other material. Thus, it is a pure HED yet was not used for mixing regolith analogs in this study. It serves as a comparison to NWA 5748. The most notable result of this heating suite is that the heated Murchison sample shows a significant increase of reflectance with respect to the unheated sample. This effect is not observed for the Phobos Simulant or for Hypersthene and the pure HEDs NWA3359 and NWA5748. While reflectances of all other heated spectra remain below their unheated counterparts for all wavelengths—though partly increasing in overall slope as well—Murchison exceeds its unheated aliquot by

far beyond ~0.6 μm. Murchison is thus the only sample that experiences a significant reddening in the VIS wavelength region.

Near Infrared Measurements of Selected Samples

For some of the samples, near-infrared (NIR) measurements at longer wavelength were acquired (requires another detector within the spectrometer). Shown is the wavelength range between 1.1 and 2.5 μm, which covers the second pyroxene absorption band centered near 1.9 μm. Beyond this range, a prominent water band is present that is not comparable to Vestan data as the water is likely adsorbed from the laboratory environment. Thus, we truncated the spectra at 2.5 μm.

In the previous sections, we observed that increasing reflectance and pyroxene band I strength (as for PIDs on

Vesta) is shown to result from the difference of heated interior and heated surface particles. In the following, spectra and spectral values are reported for the mentioned wavelength region of the samples NWA5748, NWA5748M, NWA5230M, H90P10, H80P20, and H70P30 for 400°C and 72 h (for H90P10, a measurement of the interior particles after 600°C and 72 h is shown as well). The spectral values were computed by smoothing the laboratory spectra (as they show high degrees of distortion) with the IDL smooth function and a convolution width of 40. Then, the reflectances at 1.446 and 1.910 are extracted to generate the ratio 1.446/1.910 [μm] shown in Table 4, which indicates the pyroxene absorption strength of the second major pyroxene absorption (according to the ratio 0.750/0.917 [μm] for the first pyroxene absorption) and represents the closest value to the wavelength and ratio reported for VIR data in Michalik, Stephan, et al. (2022).

Figure A1.8 shows spectra of NWA5748M, NWA 5230M, NWA5748, and Murchison. Figure A1.9 shows spectra of terrestrial regolith analogs. The corresponding spectral values (reflectance at 1.446 μm and 1.446/1.910 [μm]) are reported in Table 4 for all samples.

The general trend of increasing reflectance and pyroxene band strength continues in the NIR region for the second pyroxene absorption band. NWA 5748M and NWA 5230M both show an increase in reflectance and pyroxene band II strength for the interior versus the surface (although NWA 5230M does not show a band I strength increase). NWA5748 (without Murchison) likewise shows a slight increase in reflectance between surface particles and interior particles, yet with no increase in pyroxene band II strength. The terrestrial samples (Figure A1.9) do not exhibit an increase of pyroxene band II strength of the interior versus surface, however, data of the surface of the H90P10, 600°C, 72 h aliquot is not available. Nevertheless, the 600°C, 72 h, interior spectrum for H90P10 shows that at least the increased reflectance translates into the NIR region. H70P30 shows a slight increase in reflectance, yet without a corresponding increase in pyroxene band II strength (in contrast to its band I strength).

APPENDIX A.2: SUPPORTING RESULTS OF EMPA FINDINGS

TABLE A2.1. Detailed WDS oxide analysis.

No.	SiO_2	TiO_2	Cr_2O_3	FeO	MnO	Total	Fe_2O_3
1	0.05	0.00	0.04	89.96	0.00	90.04	99.967
2	0.11	0.00	0.08	88.99	0.00	89.19	98.895
3	0.05	0.03	0.02	88.66	0.00	88.75	98.523
4	0.20	0.00	0.02	83.19	0.05	83.45	92.445
5	0.03	0.01	0.02	86.26	0.00	86.31	95.855
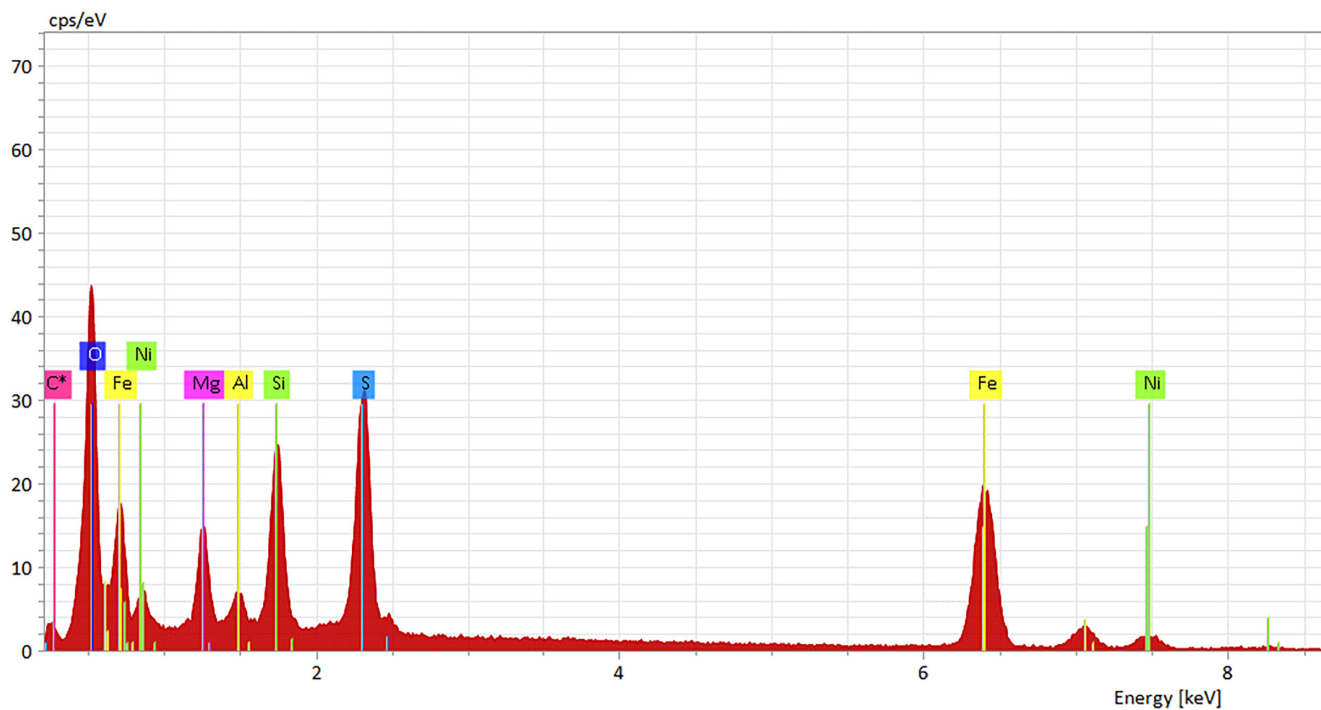
FIGURE A2.2. EDS spectrum of the sulfur-rich phase shown in Figure 5c. (Color figure can be viewed at wileyonlinelibrary.com)